Frontiers in Marine Science

TYPE Original Research
PUBLISHED 24 July 2024
DOI 10.3389/fmars.2024.1439471

EDITED BY
Guangchao Zhuang,
Ocean University of China, China

REVIEWED BY
Xiting Liu,
Ocean University of China, China
Zhiwei He,
Tongji University, China

*CORRESPONDENCE
Shao-Yong Jiang
shyjiang@cug.edu.cn

RECEIVED 28 May 2024
ACCEPTED 04 July 2024
PUBLISHED 24 July 2024

CITATION
Liu C, Jiang S-Y, Su X, Bian X, Ding H, Li D and Yang T (2024) Iron species and sulfur isotopic compositions of authigenic pyrite in deep-sea sediments at southern Hydrate Ridge, Cascadia margin (ODP Leg 204): implications for non-steady-state depositional and diagenetic processes. *Front. Mar. Sci.* 11:1439471.
doi: 10.3389/fmars.2024.1439471

Iron species and sulfur isotopic compositions of authigenic pyrite in deep-sea sediments at southern Hydrate Ridge, Cascadia margin (ODP Leg 204): implications for non-steady-state depositional and diagenetic processes

Chenhui Liu[1,2], Shao-Yong Jiang[3]*, Xin Su[4], Xiaopeng Bian[5], Hai Ding[6], Da Li[7] and Tao Yang[2]

[1]Laoshan Laboratory, Qingdao, China, [2]State Key Laboratory for Mineral Deposits Research, School of Earth Sciences and Engineering, Nanjing University, Nanjing, China, [3]State Key Laboratory of Geological Processes and Mineral Resources, School of Earth Resources, China University of Geosciences, Wuhan, China, [4]School of Ocean Sciences, China University of Geosciences, Beijing, China, [5]Department of Earth Sciences, University of Southern California, Los Angeles, CA, United States, [6]Exploration Research Institute, Anhui Provincial Bureau of Coal Geology, Hefei, China, [7]School of Marine Science and Engineering, Nanjing Normal University, Nanjing, China

Two accretionary sediment sequences from Sites 1245 and 1252 recovered during Ocean Drilling Program (ODP) Leg 204 at southern Hydrate Ridge were investigated to explore the response of geochemical partitioning of iron and sulfur isotopic composition of authigenic pyrite to non-steady-state depositional and diagenetic scenarios. Five iron species were characterized by a modified sequential extraction procedure that covers almost all iron-bearing minerals in sediment cores, including: (1) iron-bearing carbonates, mainly siderite; (2) ferric (hydr)oxides, probably ferrihydrite and/or lepidocrocite; (3) magnetite; (4) iron-bearing silicates; and (5) pyrite. Highly reactive iron has been accumulated for a long-term steady-state history and its pyritization, to varying degrees, is limited by availability of dissolved sulfide. This causes pyrite and siderite occurred in the same sedimentary layer and shows an inverse relationship between their concentrations. From this, their proportions to highly reactive iron can be chosen for evaluating the degree of sulfidization. A significant change in sulfur isotopic composition of pyrite (-42.4 to +16.8‰ VCDT) indicates that the steady-state conditions are dramatically limited, where the $\delta^{34}S$ values higher than -20‰ may result from an upward shift of SMT zone close to the seafloor or a sudden, massive depositional event. To explain the downcore sulfidization effects and pyrite $\delta^{34}S$ values, we developed two categories of conceptual scenarios based on variations in sedimentation rate and methane flux. The geochemical features similar to those derived from each scenario were searched in the sediment columns and the non-steady-state events behind the scenarios were proved to be consistent with the real observations. Thus, iron species and pyrite $\delta^{34}S$ values can be regarded as a proxy to differentiate different non-steady-state depositional and diagenetic controls on the sedimentary record.

KEYWORDS

iron species, authigenic pyrite, sulfur isotopes, non-steady-state, Hydrate Ridge, ODP Leg 204

1 Introduction

Non-steady-state depositional episodes, such as debris flows, turbidity currents, and slide/slump blocks, occur frequently in deep-sea, continental margin environments, which are often influenced by gravity and slope instability (e.g., collapse), and sometimes also result from syn- and post-depositional tectonic activities. These non-steady-state depositional events conceivably alter the physical-chemical equilibrium between sedimentary pore water and overlying seawater and thus disrupt the processes of early diagenesis (e.g., De Lange, 1983; Zabel and Schulz, 2001; Hensen et al., 2003; Fu et al., 2008; Aller et al., 2010; Liu X. et al., 2019). During uninterrupted early diagenesis, sediments and pore water will be affected by many diagenetic factors in association with the processes of physical solution transports (i.e., diffusion, advection, bioturbation, and irrigation) and chemical reactions (e.g., Borowski et al., 1996; Fossing et al., 2000; Dickens, 2001; Chatterjee et al., 2011). Pore water geochemical models were used to recognize and recover the non-steady-state depositional and diagenetic events occurred recently (e.g., Dickens, 2001; Zabel and Schulz, 2001; Hensen et al., 2003; Paull et al., 2005). These studies estimated that pore water profiles adjust to a new depositional or diagenetic condition within hundreds or thousands of years, which is very short compared to the history of burial and mineralization in the sediment column. Thus, pore water models are exceedingly difficult for reconstructing more ancient non-steady-state events.

Geochemical pathways of iron and sulfur during early diagenesis have been well studied (see below and Figure 1). Nevertheless, constrained by the limited sampling depths (e.g., no penetration over the sulfate reduction zone) or the absence of relevant depositional and diagenetic data, the impacts of non-steady-state events on pyritization is still rarely studied and poorly understood. Fu et al. (2008) proposed two conceptual non-steady-state depositional models to explain the greigite formation in Quaternary sediments from Gulf of Mexico. However, they only emphasized the incipient pyritization and neglected the quantification of authigenic pyrite. Considering the complexity of actual situations, these non-steady-state models are dramatically limited since disruptive early diagenesis is common on continental margin.

Sulfate-methane transition (SMT) zone is a diffusion-controlled boundary not only separating sulfate reduction above and methanogenesis below, but also characterizing a mutual depletion of methane and sulfate by anaerobic oxidation of methane (AOM) (e.g., Reeburgh, 1980; Devol and Ahmed, 1981; Iversen and Jørgensen, 1985; Treude et al., 2003). Under steady-state conditions, authigenic pyrite formed in the SMT zone is characterized as heavier sulfur isotopic compositions than those formed above in the sulfate reduction zone (e.g., Jørgensen et al., 2004; Borowski et al., 2013; Lin et al., 2016). Given that position of the SMT zone will shift if the stability of early diagenesis is destroyed, sulfur isotope variation of pyrite in the sediment column would serve as an indirect clue to non-steady-state depositional and diagenetic history.

In this study, we aimed to understand the response of geochemical partitioning of iron and sulfur isotope composition of authigenic pyrite to non-steady-state depositional and diagenetic scenarios. As one of the most famous gas hydrate-bearing regions, southern Hydrate Ridge was specifically targeted for Ocean Drilling Program (ODP) during Leg 204 (Tréhu et al., 2003). Many researches involving lithology, sedimentology, geophysics, and geochemistry, etc. have been performed on the sites from this leg (e.g., Torres et al., 2004; Tréhu et al., 2004; Bangs et al., 2005; Tréhu et al., 2006a and references therein; Larrasoaña et al., 2007; Chatterjee et al., 2011). These data suggested that sediments at southern Hydrate Ridge have undergone a complex tectonic, depositional, and diagenetic history, which makes it suitable for the purpose of this study. In this research, we adopted a modified sequential extraction procedure (Liu C. et al., 2019) to characterize different iron species in sediment cores at Sites 1245 and 1252, and determined the factors limiting pyritization through the entire depositional history. To explain the geochemical relationship between pyrite and siderite and sulfur isotope variation of pyrite, we derived two categories of conceptual scenarios based on variations in sedimentation rate and methane flux, and then applied them to the real observations.

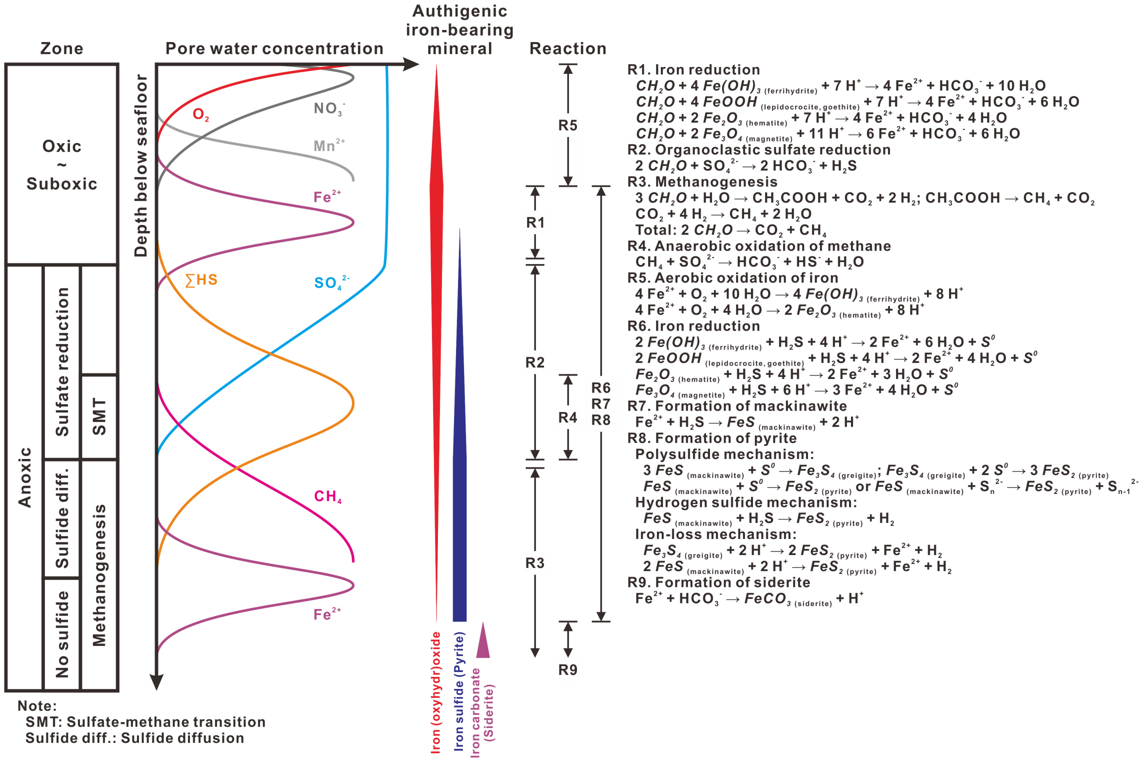

FIGURE 1
Idealized depth dependence of geochemical zonation, pore-water species, and authigenic iron-bearing minerals under early diagenetic conditions. The oxic and suboxic zones are combined here. Vertical bars in the middle represent the depth intervals where authigenic iron-bearing minerals are expected to occur, and their width variations reflect production (wider) or dissolution (narrower). Major reactions and the depth intervals where they occur are listed on the right. Modified from Goldhaber and Kaplan (1974), Barnes and Goldberg (1976), Froelich et al. (1979), Berner (1981), Goldhaber (2003); Poulton et al. (2004); Rickard and Morse (2005); Roberts and Weaver (2005); Yamaguchi et al. (2005); Jørgensen and Kasten (2006); Fu et al. (2008); Regnier et al. (2011); Roberts (2015); and references therein.

2 Geochemical pathways of iron and sulfur during early diagenesis

Before the following text, we summarized a typical scheme for geochemical pathways of iron and sulfur during early diagenesis (Figure 1) to provide a framework for further interpretation and discussion.

With progressive sediment burial, particle organic carbon will be decomposed and mineralized in an order of decreasing energy yield of external oxidants (electron acceptors): oxygen (O_2), nitrate (NO_3^-), manganese oxides (e.g., MnO_2), iron oxides (e.g., FeO(OH)), and sulfate (SO_4^{2-}). When all the electron acceptors are consumed, methanogenesis proceeds through aceticlastic fermentation and carbon dioxide reduction. From this, a series of redox-driven geochemical zones are characterized in the sediment column (Froelich et al., 1979; Berner, 1981). Reductions of iron and sulfur start in the suboxic and anoxic zones, respectively, and proceed until available solid phase ferric iron (e.g., FeO(OH)) and pore water sulfate are exhausted. Progressive consumptions of these two oxidants (electron acceptors) liberate ferrous iron (Fe^{2+}) and dissolved sulfide ($\Sigma HS = H_2S + HS^- + S^{2-}$). Upward diffusing of ferrous iron may meet with oxygen and then be oxidized and precipitated back to (oxyhydr)oxide minerals (e.g., Yamaguchi et al., 2005). In the anoxic zone, solid phase ferric minerals are also reduced by reaction with dissolved sulfide (e.g., Canfield et al., 1992; Poulton et al., 2004). Metastable iron monosulfides, such as mackinawite (ca. tetragonal FeS), tend to be formed when dissolved sulfide and ferrous iron combine, and eventually to be transformed into pyrite (FeS_2) (e.g., Goldhaber and Kaplan, 1974; Goldhaber, 2003; Rickard and Morse, 2005; Jørgensen and Kasten, 2006; Fu et al., 2008; Roberts, 2015). Greigite (cubic Fe_3S_4) and pyrrhotite (e.g., hexagonal Fe_7S_8) are also formed as metastable precursors to pyrite (e.g., Sweeney and Kaplan, 1973; Wilkin and Barnes, 1996) and most likely preserved as a result of limited production of dissolved sulfide that prevents completion of pyritization (e.g., Kao et al., 2004; Novosel et al., 2005; Roberts and Weaver, 2005; Horng and Chen, 2006; Larrasoaña et al., 2007; Fu et al., 2008). Below the sulfate reduction zone, ferrous iron reappears in the pore water profile as dissolved sulfide is gradually exhausted, and then reacts with dissolved inorganic carbon ($\Sigma CO_2 = CO_2 + HCO_3^- + CO_3^{2-}$) to precipitate iron-bearing carbonate minerals, such as siderite ($FeCO_3$) (e.g., Roberts and Weaver, 2005; Yamaguchi et al., 2005; Larrasoaña et al., 2007; Liu et al., 2023).

This geochemical scheme provides an idealized framework of diagenetic stages where different authigenic iron-bearing minerals are expected to be produced or dissolved. But, as shown below, this steady-state sequence of mineralization is commonly disrupted by the complicated marine conditions.

3 Geological setting and study sites

Juan de Fuca plate is being subducted obliquely beneath the North American plate at a rate of ca. 4.5 cm yr^{-1} (e.g., Mackay et al., 1992) (Figure 2A). Cascadia accretionary complex is evolved in response to this subduction and deformed by several active west-northwest-trending left-lateral strike-slip faults (e.g., Wecoma, Daisy Bank, and Alvin Canyon), building a series of north-south subparallel thrust faults and ridges (e.g., Mackay et al., 1992; Mackay, 1995; Goldfinger et al., 1996). As part of the second accretionary thrust ridge away from deformation front, Hydrate Ridge is a 25 km long and 15 km wide ridge located on lower continental slope ca. 90 km offshore of central Oregon, USA. Sites 1245 and 1252 of ODP Leg 204 are located on the western flank of southern Hydrate Ridge, ca. 3 km northwest of the southern summit and on the northwestern flank of Hydrate Ridge Basin-East, ca. 4.5 km northeast of the southern summit, respectively (Figure 2B).

Based on variations in sedimentological and lithologic parameters etc., sedimentary sequences recovered at Sites 1245 and 1252 were classified into five and three lithostratigraphic units (abbreviated as Units below), respectively (Shipboard Scientific Party, 2003b, 2003c) (Figure 2C). Seismic reflection survey and biostratigraphy determination (Figure 2C) showed that early Pleistocene to Holocene (ca. 1.6 to 0 Ma) sediments are folded and uplifted into an asymmetric anticline, which

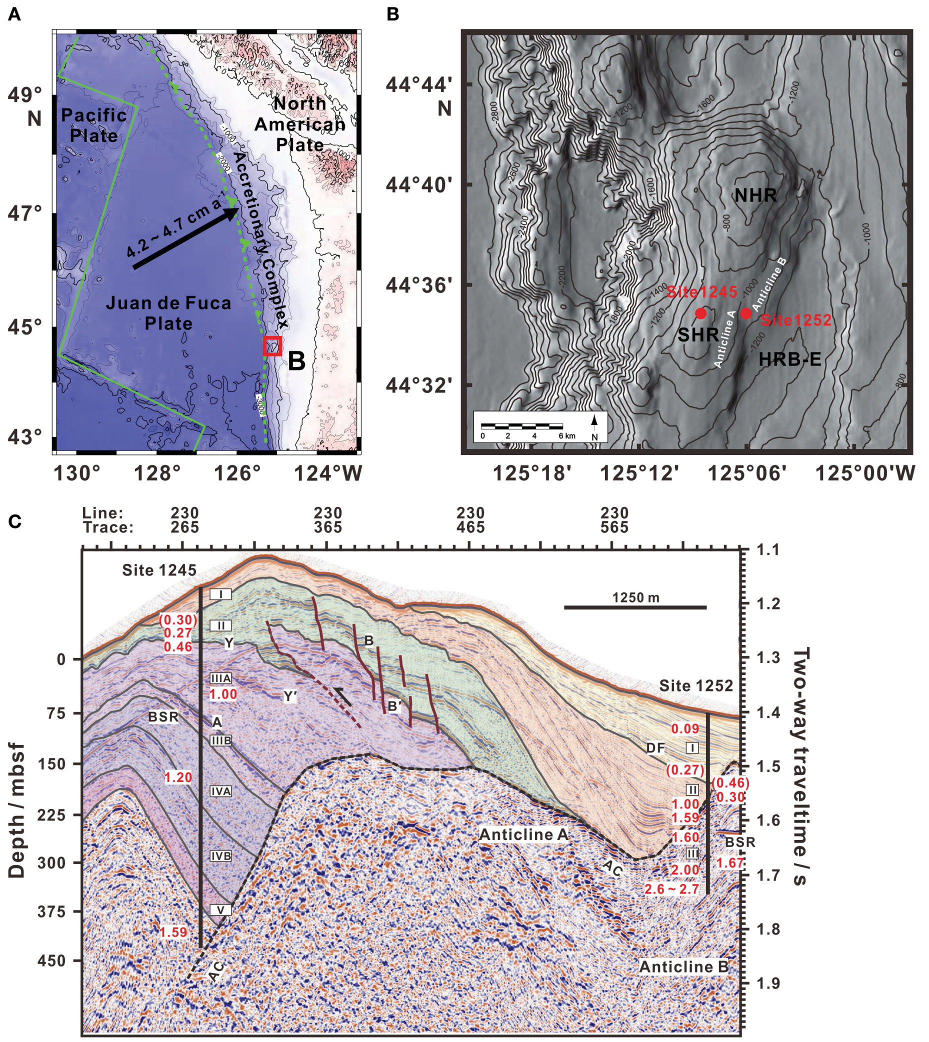

FIGURE 2
(A) Rough bathymetric map and plate tectonic setting of the Cascadia convergent margin. Red box shows region of **(B)**. **(B)** Detailed bathymetric map of the Hydrate Ridge vicinity, including northern Hydrate Ridge (NHR), southern Hydrate Ridge (SHR), Hydrate Ridge Basin-East (HRB-E), and two anticlines (Anticlines A and B). Red dots show the locations of Site 1245 (ca. 870 m) and Site 1252 (ca. 1040 m) on ODP Leg 204. **(C)** East-west vertical profile through three-dimensional seismic data across Sites 1245 and 1252. Vertical black bars show site locations and drilled depths. Colored overlays show lithostratigraphic (sub)units labeled by black letters in rectangles. Biostratigraphic ages determined by Shipboard Scientific Party (2003b, 2003c) and re-examined by Watanabe (2006), in millions of years (Ma), are shown as red numbers. Ages in parentheses are not compatible with sedimentary sequence and attributed to reworking of sediments. Important seismic reflections (Horizons A, B, B′, Y, Y′, and AC), bottom-simulating reflector (BSR), massive debris flows (DF), small-offset normal faults (red brown solid curves), thrust fault (red brown dashed curve), and Anticlines A and B are also shown. Modified from Shipboard Scientific Party (2003a); Chevallier et al. (2006); Johnson et al. (2006); and Tréhu et al. (2006b).

unconformably overlies a low-frequency incoherent facies interpreted to be an older (> 1.0 Ma) and highly deformed accretionary complex as the core of Hydrate Ridge (Shipboard Scientific Party, 2003a; Chevallier et al., 2006). When compared to the summit and western flank of southern Hydrate Ridge, sediments on the northwestern flank of Hydrate Ridge Basin-East appear to be less deformed (Shipboard Scientific Party, 2003a, 2003c). Inconsistencies between biostratigraphic age and sedimentary sequence observed in Unit II at Site 1245 and in Units I and II at Site 1252 (ages in parentheses in Figure 2C) would be due to re-deposition of sediments caused by massive debris flows (labeled as DF in Figure 2C) and slope instability, respectively (Chevallier et al., 2006; Watanabe, 2006).

Bottom-simulating reflector (BSR) is present everywhere through Site 1245 and the summit until the location near Site 1252, but reappears to the east within the core of Anticline B (Shipboard Scientific Party, 2003a) (Figure 2C). Gas hydrate distributes dispersedly with estimated concentrations of 3 to 4 vol % of pore space between 40 mbsf and the BSR depth (ca. 134 mbsf) at Site 1245, but the concentrations decrease to less than 2 vol% at Site 1252 (Torres et al., 2004; Tréhu et al., 2004, 2006b). At Sites 1245 and 1252, neither fault nor high permeable sedimentary layer is existed as a fluid conduit towards the seafloor, and thus nowadays methane can only be diffused upward and then depleted before reaching the seafloor by AOM. The present-day SMT zones at Sites 1245 and 1252 are located at ca. 7 mbsf and ca. 5 mbsf, respectively (Shipboard Scientific Party, 2003b, 2003c).

4 Materials and methods

Sediment samples collected from Sites 1245 (Hole 1245B; 44° 35.1587′N, 125°8.9455′W; 869.7 m water depth) and 1252 (Hole 1252A; 44°35.1671′N, 125°5.5691′W; 1039.3 m water depth) are composed of hemipelagic clays and silty clays, locally interbedded with silty- to sandy-rich turbidites (Shipboard Scientific Party, 2003b, 2003c). According to an improved method as described by Liu C. et al. (2019), five solid-phase iron species were extracted sequentially and further characterized as different combinations of iron-bearing minerals: (1) Acetate-extractable iron (Fe_A): iron-bearing carbonates, such as siderite ($FeCO_3$), and metastable iron sulfides, including mackinawite (ca. FeS), greigite (Fe_3S_4), and pyrrhotite (e.g., Fe_7S_8); (2) Dithionite-extractable iron (Fe_D): ferric (hydr)oxides, including ferrihydrite (ca. $Fe(OH)_3$), lepidocrocite (γ-FeO(OH)), goethite (α-FeO(OH)), and hematite (Fe_2O_3); (3) Oxalate-extractable iron (Fe_O): magnetite (Fe_3O_4); (4) Hydrofluoric acid-extractable iron (Fe_{HF}): iron-bearing silicates; and (5) Nitric acid-extractable iron (Fe_{HNO3}): pyrite (FeS_2). Total iron (Fe_T) concentration was equal to the sum of all five iron species extracted here ($Fe_T = Fe_A + Fe_D + Fe_O + Fe_{HF} + Fe_{HNO3}$).

Two reduced solid-phase sulfur species, acid volatile sulfur (S_{AV}) and chromium reducible sulfur (S_{CR}), were extracted sequentially using distillation technique (e.g., Canfield et al., 1986; Bates et al., 1993; Backlund et al., 2005; Gröger et al., 2009; Liu C. et al., 2019). The species of S_{AV} and S_{CR} were extracted by boiled hydrochloric acid and hot chromium (II) chloride, respectively. Hydrogen sulfide released by both was quantitatively trapped as silver sulfide (Ag_2S). Most of metastable iron sulfides, including 100% of mackinawite, 75% of greigite, and an unknown proportion of pyrrhotite, can be extracted as S_{AV} (Cornwell and Morse, 1987). All the reduced sulfur-bearing minerals survived from S_{AV} extraction, including pyrite and elemental sulfur (S^0), are further reduced as S_{CR} (Canfield et al., 1986; Gröger et al., 2009).

Stable sulfur isotope analyses were performed in the Key Laboratory of Nuclear Resources and Environment, Ministry of Education at the East China Institute of Technology, using a Finnigan MAT 253 isotopic ratio mass spectrometer connected with a Flash EA 1112 elemental analyzer via a Finnigan Conflo II open split interface. Circa 2 mg of Ag_2S obtained from S_{CR} extraction was wrapped into a small tin capsule and then combusted with cuprous oxide at 1020°C to produce sulfur dioxide for isotopic ratio measurement. Due to a very small amount of Ag_2S recovered after filtration during S_{AV} extraction, its sulfur isotopes were not analyzed here. All the isotope data were reported in conventional delta notation ($\delta^{34}S$) as per mille (‰) deviation relative to the Vienna Cañon Diablo troilite (VCDT) standard (Beaudoin et al., 1994) with reproducibility of 0.2‰ (1SD). Working standards used here were two Chinese sulfur isotopic reference materials GBW04414 and GBW04415, whose $\delta^{34}S$ values are -0.07 ± 0.13‰ and +22.15 ± 0.14‰, respectively (Ding et al., 2001).

5 Results and discussion

5.1 Concentrations of extracted species and confirmation of their recognized minerals

Concentration results of all extracted species for Sites 1245 and 1252 are listed in Table 1, which include Fe_A, Fe_D, Fe_O, Fe_{HF}, Fe_{HNO3}, S_{AV}, and S_{CR}. Depth profiles of these data are shown in Figure 3. At Site 1245, concentrations of Fe_A, Fe_{HNO3}, and S_{CR} show a large and frequent fluctuation throughout Units I to III (1SD: 0.16 wt% of Fe_A, 0.07 wt% of Fe_{HNO3}, and 0.10 wt% of S_{CR}) but become stable below (1SD: 0.08 wt% of Fe_A, 0.02 wt% of Fe_{HNO3}, and 0.03 wt% of S_{CR}). Throughout Unit IV, concentrations of Fe_{HNO3} and S_{CR} drop to minimum levels (0.02 ~ 0.09 wt% of Fe_{HNO3} and 0.01 ~ 0.10 wt% of S_{CR}), whereas Fe_A increases to maximum levels (0.51 ~ 0.81 wt%). In contrast, concentrations of Fe_D, Fe_O, and Fe_{HF} keep relatively stable throughout the whole profile (1RSD < 18%). At Site 1252, except for Fe_{HF} (1RSD < 8%), other species appear to be heterogeneous with depth (1RSD: 37% of Fe_A, 36% of Fe_D, 14% of Fe_O, 90% of Fe_{HNO3}, and 94% of S_{CR}), especially in Unit III where concentrations of Fe_A, Fe_D, Fe_{HNO3}, and S_{CR} are more scattered (1RSD: 50% of Fe_A, 38% of Fe_D, 97% of Fe_{HNO3}, and 101% of S_{CR}). Concentrations of S_{AV} at these two sites are generally below the detection limit, though most samples having just detectable S_{AV} were collected from Unit IV of Site 1245 (0.0002 ~ 0.003 wt%).

Characterization of the extracted species indicates that Fe_{HNO3} is equal to pyrite iron while S_{CR} consists of both pyrite sulfur and elemental sulfur. If S_{CR} only includes pyrite sulfur, the atomic S_{CR}/

TABLE 1 Concentrations of extracted fractions (Fe_A, Fe_D, Fe_O, Fe_{HF}, Fe_{HNO3}, S_{AV}, and S_{CR}) and sulfur isotopic compositions of S_{CR} ($\delta^{34}S_{CR}$) at Sites 1245 and 1252.

Core, section, interval (cm)	Depth (mbsf)	Fe_A (wt%)	Fe_D (wt%)	Fe_O (wt%)	Fe_{HF} (wt%)	Fe_{HNO3} (wt%)	S_{AV} (wt%)	S_{CR} (wt%)	$\delta^{34}S_{CR}$ (‰ VCDT)
ODP204–1245B-									
1H-2, 130–132	2.80	0.183	0.244	0.506	2.722	0.191	BDL	0.221	-12.43
1H-5, 95–97	6.95	0.203	0.270	0.468	2.551	0.239	BDL	0.267	-20.98
2H-1, 10–12	9.60	0.184	0.298	0.508	2.670	0.246	BDL	0.289	-18.05
3H-1, 15–17	19.15	0.222	0.285	0.532	2.635	0.212	BDL	0.326	-1.89
3H-5, 120–122	26.20	0.386	0.407	0.577	2.733	0.094	BDL	0.123	-18.81
4H-1, 20–22	28.70	0.484	0.413	0.530	2.467	0.072	0.0005	0.071	-25.82
4H-5, 30–32	34.80	0.565	0.420	0.592	2.706	0.025	BDL	0.029	-18.69
5H-5, 15–17	44.15	0.390	0.387	0.654	2.795	0.237	BDL	0.335	-2.20
6H-2, 130–132	50.30	0.357	0.386	0.622	2.812	0.080	BDL	0.088	-22.77
6H-5, 55–57	54.05	0.328	0.334	0.584	2.636	0.275	BDL	0.321	-38.33
7H-2, 47–49	58.02	0.283	0.346	0.645	FA	0.240	BDL	0.347	-30.74
8H-2, 120–122	69.20	0.337	0.352	0.641	2.924	0.059	BDL	0.060	-21.22
8H-7, 40–42	75.76	0.281	0.320	0.565	2.298	0.148	BDL	0.170	-26.39
9H-2, 85–87	78.17	0.348	0.367	0.626	2.396	0.138	BDL	0.171	-14.75
10H-2, 93–95	87.93	0.614	0.469	0.633	2.728	0.019	0.0003	0.027	-10.17
10H-5, 32–34	91.45	0.442	0.359	0.665	2.643	0.081	BDL	0.113	-14.13
11H-2, 120–122	97.17	0.300	0.413	0.728	2.925	0.033	BDL	0.023	-28.99
12H-2, 93–95	106.90	0.464	0.334	0.639	2.441	0.170	BDL	0.215	+12.95
12H-5, 80–82	111.27	0.544	0.286	0.497	1.963	0.124	0.0084	0.155	+13.00
13H-2, 90–92	116.40	0.635	0.535	0.734	2.918	0.045	0.0468	0.123	-1.85
14H-2, 10–12	124.20	0.390	0.314	0.628	2.612	0.134	BDL	0.175	-16.72
15X-4, 30–32	131.16	0.455	0.361	0.691	2.976	0.032	BDL	0.024	-35.62
16X-3, 100–102	141.50	0.474	0.359	0.600	2.566	0.119	BDL	0.135	-32.65
17P-1, 8–10	147.18	0.512	0.313	0.730	2.791	0.103	BDL	0.110	-31.92
18X-3, 15–17	152.13	0.846	0.441	0.943	2.880	0.006	BDL	0.010	-10.50
19X-2, 110–112	159.60	0.304	0.396	0.706	2.801	0.147	BDL	0.182	-18.73
20X-3, 100–102	170.50	0.280	0.372	0.650	FA	0.130	BDL	0.177	-29.66
21X-1, 14–16	176.24	0.305	0.310	0.763	2.788	0.162	BDL	0.218	-27.52
21X-3, 90–92	179.92	0.332	0.244	0.481	1.892	0.087	BDL	0.095	-19.09
22X-1, 130–132	186.70	0.329	0.287	0.634	2.539	0.121	BDL	0.135	-6.38
23X-6, 10–12	202.30	0.671	0.308	0.650	2.765	0.065	BDL	0.049	-15.38
24X-2, 110–112	206.80	0.610	0.384	0.756	2.890	0.051	BDL	0.044	-33.46
25X-2, 110–112	216.59	0.625	0.421	0.786	2.684	0.033	BDL	0.026	-24.01
28X-2, 105–107	245.48	0.628	0.380	0.929	2.659	0.022	BDL	0.015	-24.69
29X-2, 104–106	255.14	0.510	0.367	0.790	2.953	0.041	BDL	0.032	-25.76

(Continued)

TABLE 1 Continued

Core, section, interval (cm)	Depth (mbsf)	Fe_A (wt%)	Fe_D (wt%)	Fe_O (wt%)	Fe_{HF} (wt%)	Fe_{HNO3} (wt%)	S_{AV} (wt%)	S_{CR} (wt%)	$\delta^{34}S_{CR}$ (‰ VCDT)
30X-2, 110–112	264.80	0.601	0.322	0.922	2.797	0.076	BDL	0.070	-37.92
31X-6, 10–12	279.11	0.650	0.331	0.811	3.023	FA	0.0005	0.057	-19.21
32X-2, 112–114	284.12	0.800	0.359	0.844	2.820	0.038	BDL	0.032	-16.12
34X-2, 100–102	295.70	0.677	0.356	0.782	2.695	0.020	0.0026	0.020	-22.09
35X-2, 105–107	303.35	0.776	0.397	0.815	2.582	0.018	0.0020	0.019	-14.68
36X-2, 100–102	312.90	0.812	0.274	0.700	2.806	0.039	0.0019	0.035	-22.53
37X-2, 104–106	322.54	0.666	0.347	0.610	2.866	0.048	0.0002	0.047	-22.32
38X-4, 133–135	335.53	0.699	0.435	0.868	3.050	0.016	0.0032	0.019	-12.47
40X-2, 100–102	351.40	0.737	0.447	0.814	FA	0.038	0.0002	0.049	-25.30
42X-2, 105–107	370.75	0.751	0.417	0.723	3.077	0.044	0.0006	0.044	-31.24
43X-3, 120–122	382.00	0.652	0.302	0.852	3.340	0.080	0.0009	0.077	-25.15
44X-2, 100–102	389.90	0.638	0.295	0.722	3.122	0.094	0.0004	0.101	-33.27
45X-2, 105–107	399.65	0.659	0.367	0.832	2.907	0.047	BDL	0.052	-26.74
47X-2, 104–106	409.59	0.678	0.324	0.824	2.989	0.086	0.0012	0.092	-24.18
ODP204–1252A-									
1H-1, 50–52	0.50	0.308	0.383	0.809	2.665	0.324	BDL	0.377	-36.79
1H-1, 110–112	1.10	0.359	0.433	1.091	2.683	0.237	BDL	0.371	-30.98
1H-2, 110–112	2.60	0.281	0.448	1.078	2.643	0.280	BDL	0.495	+3.57
1H-3, 45–47	3.45	0.219	0.288	0.826	2.856	0.245	0.0015	0.320	+7.05
2H-1, 5–7	4.95	0.394	0.447	1.136	2.717	0.610	BDL	1.189	-20.46
2H-2, 18–20	6.58	0.261	0.360	1.020	2.799	0.177	BDL	0.250	-23.02
2H-4, 120–122	10.60	0.395	0.454	1.156	2.789	0.205	FA	0.422	-29.26
3H-2, 110–112	15.75	0.359	0.325	1.038	2.669	0.107	FA	0.244	-18.94
4H-2, 55–57	25.95	0.484	0.597	1.212	2.619	0.065	BDL	0.095	-2.67
4H-5, 13–15	29.91	0.477	0.448	1.104	2.543	0.142	BDL	0.239	-17.45
5H-2, 53–55	34.52	0.343	0.396	0.832	2.724	0.130	BDL	0.149	-26.15
6H-2, 56–58	44.96	0.372	0.428	1.097	2.677	0.075	BDL	0.076	-24.02
6H-4, 10–12	47.50	0.303	0.336	0.930	2.953	0.137	BDL	0.153	-35.19
7H-2, 106–108	54.96	0.329	0.377	0.890	3.233	0.139	BDL	0.203	-13.61
7H-4, 105–107	57.95	0.423	0.476	1.026	3.315	0.054	BDL	0.079	-5.32
8H-6, 10–12	69.50	0.433	0.401	1.236	2.987	0.083	BDL	0.154	-15.77
9H-3, 90–92	75.30	0.335	0.465	0.955	2.912	0.115	BDL	0.125	-13.05
10H-3, 15–17	83.15	0.505	0.415	0.966	2.744	0.205	BDL	0.230	-12.76
11H-2, 110–112	93.00	0.303	0.456	0.832	3.121	0.162	BDL	0.190	-39.25
11H-5, 5–7	96.45	0.284	0.406	1.049	3.357	0.095	BDL	0.124	-19.40
12H-4, 100–102	105.30	0.428	0.474	0.875	2.839	0.129	BDL	0.171	-0.00

(Continued)

TABLE 1 Continued

Core, section, interval (cm)	Depth (mbsf)	Fe_A (wt%)	Fe_D (wt%)	Fe_O (wt%)	Fe_{HF} (wt%)	Fe_{HNO3} (wt%)	S_{AV} (wt%)	S_{CR} (wt%)	$\delta^{34}S_{CR}$ (‰ VCDT)
13H-4, 10–12	114.00	0.414	0.372	0.826	2.911	0.076	BDL	0.091	-19.28
14H-2, 117–119	121.57	0.262	0.661	1.004	3.006	0.188	BDL	0.283	-32.88
14H-5, 88–90	125.70	0.240	0.732	0.798	2.979	0.031	BDL	0.050	-16.70
14H-6, 130–132	127.39	0.273	0.364	0.719	3.103	0.265	BDL	0.306	-32.79
15X-3, 95–97	128.95	0.150	0.949	0.941	2.837	0.035	BDL	0.040	-20.24
15X-6, 30–32	132.68	0.252	0.334	0.857	3.159	0.436	BDL	0.526	-9.40
16X-2, 108–110	137.28	0.153	0.954	0.839	2.744	0.044	BDL	0.057	-20.41
16X-4, 88–90	140.08	0.122	0.916	0.935	2.785	0.044	BDL	0.067	-28.53
17X-2, 105–107	146.95	0.143	0.835	1.242	2.897	0.047	BDL	0.061	-9.89
18X-5, 34–36	160.14	0.255	0.477	0.887	3.212	0.108	BDL	0.116	-30.05
19X-1, 115–117	164.95	0.262	0.425	0.922	3.282	0.089	BDL	0.106	-32.84
19X-6, 10–12	171.40	0.376	0.495	1.142	3.065	0.124	BDL	0.203	+10.21
20X-2, 110–112	176.10	0.294	0.404	1.038	3.108	0.234	BDL	0.292	-37.16
20X-4, 90–92	178.90	0.292	0.370	0.965	3.130	0.297	BDL	0.318	-42.36
21X-2, 20–22	184.80	0.330	0.423	0.969	2.920	0.579	BDL	0.693	-24.21
22X-3, 110–112	196.80	0.405	0.560	1.162	2.706	0.932	BDL	1.145	+16.84
23X-3, 15–17	204.63	0.577	0.725	1.026	3.166	0.158	0.0004	0.256	-3.21
24X-2, 110–112	213.80	0.829	0.720	0.948	3.105	0.086	0.0021	0.099	-21.19
25X-2, 118–120	223.58	0.405	0.427	1.000	3.181	0.249	BDL	0.266	-20.97
26X-3, 115–117	234.65	0.229	0.805	0.814	2.424	0.039	BDL	0.036	-30.06
27X-3, 115–117	244.35	0.301	0.307	0.764	3.028	0.249	BDL	0.283	-38.41
28X-5, 73–75	256.57	0.281	0.358	0.787	2.975	0.380	BDL	0.422	-39.90

BDL, below detection limit; FA, failed analysis.

Fe_{HNO3} ratio will be close to 2. The addition of elemental sulfur will bias the atomic S_{CR}/Fe_{HNO3} ratio to a higher value than 2. A plot of Fe_{HNO3} versus S_{CR} exhibits a strong linear correlation ($R^2 = 0.95$) with a slope of 2.16 (Figure 4A), indicating that pyrite sulfur is the dominant fraction of S_{CR} and elemental sulfur accounts for only a minor fraction (Liu C. et al., 2019). Therefore, Fe_{HNO3} and S_{CR} represent the actual concentrations of pyrite iron and sulfur in sediments, respectively.

Larrasoaña et al. (2006, 2007) carried out a detailed research on ODP Leg 204 core sediments with rock magnetic identification and electron microscope observation, which provides some evidence to constrain and confirm the recognition of species extracted here:

- Ratio of the isothermal remanent magnetization at a field of 0.9 T to the magnetic susceptibility (IRM@0.9T/χ) greater than 15 kA m^{-1} is due to the presence of greigite and pyrrhotite. These two metastable sulfide minerals were extracted as S_{AV}, which concentrations are generally above the detection limit at depths where IRM@0.9T/χ ratio is higher than 13.5 kA m^{-1}, especially in Unit IV at Site 1245 (Figure 3). The limited amounts of S_{AV}, however, suggest that the concentration levels of greigite and pyrrhotite, if present, are much lower than those of pyrite. Similar results were also obtained from ODP Sites 888, 889, and 890 to the north of Hydrate Ridge in Cascadia Margin, not far from our studied sites, where little or no S_{AV} was extracted (Bottrell et al., 2000).
- Pyrrhotite is observed to occur invariably associated with siderite. Similar association between greigite and siderite was also observed by Roberts and Weaver (2005). When comparing Fe_A with IRM@0.9T/χ ratio, it is notable that concentrations of Fe_A are lower than 0.5 wt% in most magnetite-dominated samples (IRM@0.9T/χ < 13.5 kA m^{-1}), but tend to rise (0.48 ~ 0.85 wt%) in the samples containing greigite and/or pyrrhotite (IRM@0.9T/χ: 13.5 ~ 128 kA m^{-1}) (Figure 4B). Because both greigite and pyrrhotite are at low concentrations as confirmed by S_{AV} extraction, their amounts are insufficient to increase Fe_A concentrations (the maximum concentration of S_{AV} contributes less than 0.1 wt% of Fe_A).

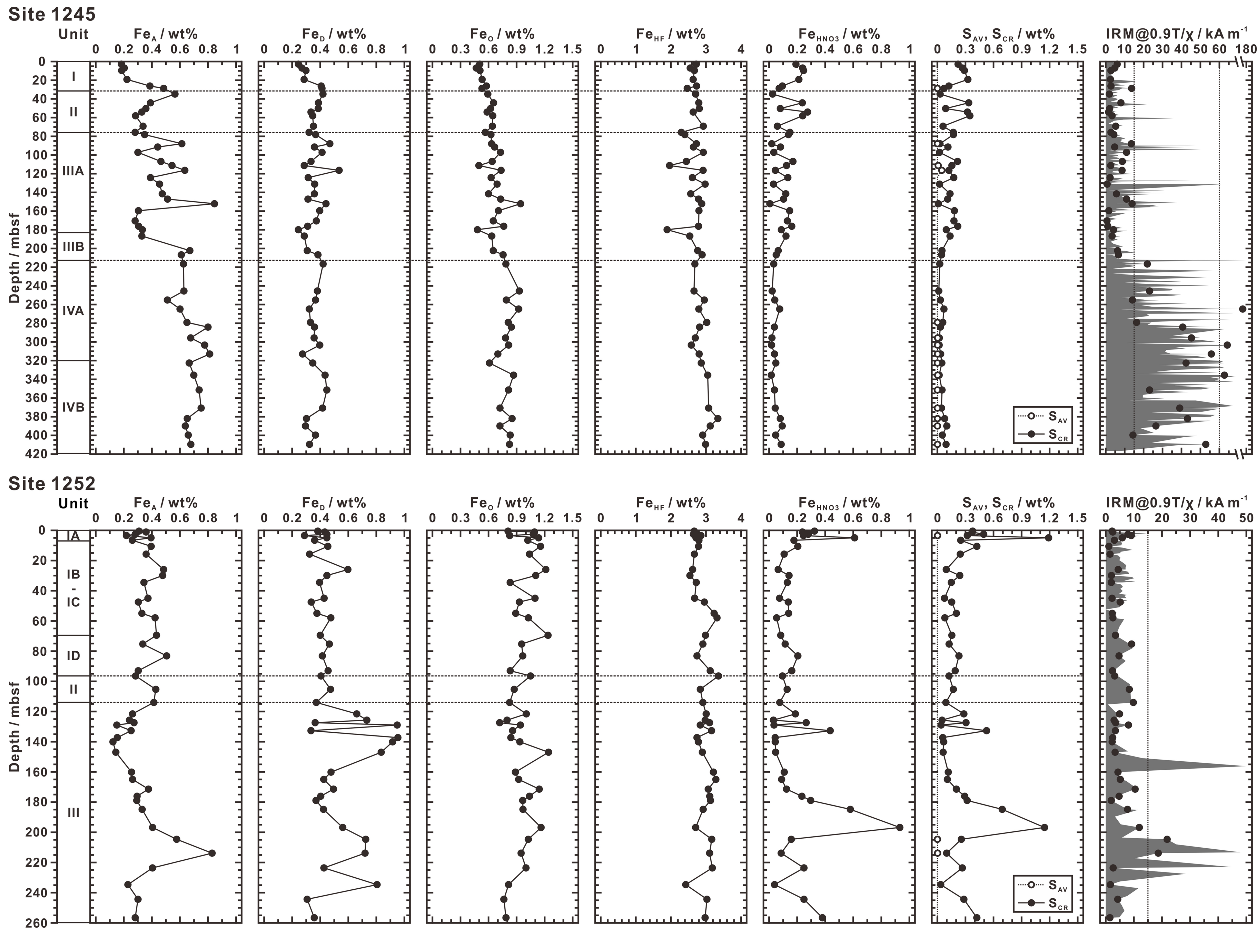

FIGURE 3

Profiles of concentrations of extracted fractions (Fe$_A$, Fe$_D$, Fe$_O$, Fe$_{HF}$, Fe$_{HNO3}$, S$_{AV}$, and S$_{CR}$) with depth and lithostratigraphic (sub)unit at Sites 1245 and 1252. Data of IRM@0.9T/χ ratio shown in the rightmost profiles (black circles represent the samples as same as those used in this study) are given by Larrasoaña et al. (2006, 2007) and Luo et al. (2013), which is generally used to identify the presence of greigite (> 15 kA m^{-1}) and pyrrhotite (> 60 kA m^{-1}). The column Unit represents lithostratigraphic (sub)unit.

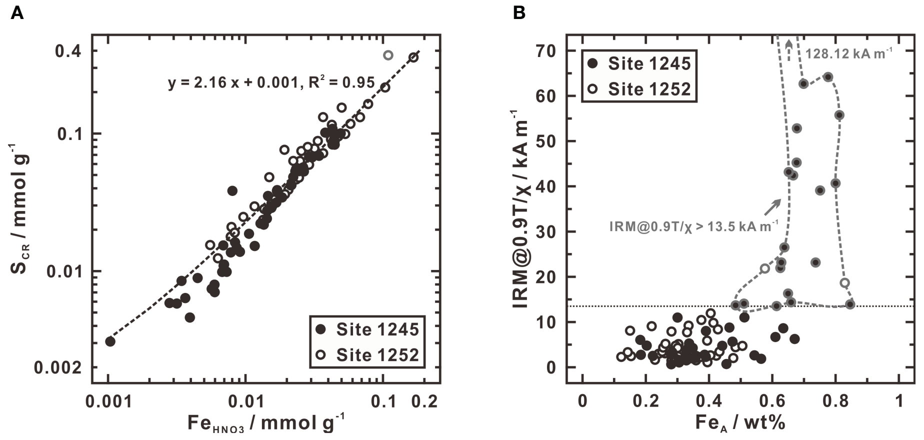

FIGURE 4

Plots of Fe$_{HNO3}$ versus S$_{CR}$ **(A)** and Fe$_A$ versus IRM@0.9T/χ **(B)** at Sites 1245 and 1252. In **(A)**, the concentrations of Fe$_{HNO3}$ and S$_{CR}$ are clearly linearly related. Note the lone circle outlined in gray at top right. If this point is included in least-squares fitting, the slope of the best-fit line is 2.3; if not used the slope is 2.16. In **(B)**, the gray outlined circles (enclosed in gray dashed line) show the samples with IRM@0.9T/χ ratios higher than 13.5 kA m^{-1}, in which greigite and/or pyrrhotite are contained (Larrasoaña et al., 2006, 2007). Data of IRM@0.9T/χ ratio are given by Luo et al. (2013).

That is to say, Fe_A should be approximately equal to carbonate-associated iron and siderite may be its most likely mineral form.
- Thermal demagnetization data suggest the predominance of magnetite and the absence of goethite and hematite. These results not only confirm the iron source of Fe_O but also constrain that Fe_D may be largely extracted from other ferric (hydr)oxide phases, probably ferrihydrite or lepidocrocite.

As recognized and confirmed above, our extracted species at Sites 1245 and 1252 are summarized as follows: (1) Fe_A: iron-bearing carbonates, mainly siderite; (2) Fe_D: ferric (hydr)oxides, probably ferrihydrite and/or lepidocrocite; (3) Fe_O: magnetite; (4) Fe_{HF}: iron-bearing silicates; (5) Fe_{HNO3}: pyrite; (6) S_{AV}: greigite and/or pyrrhotite; and (7) S_{CR}: pyrite.

5.2 Limitation of pyritization and classification of sulfidization degrees

In marine sediments on continental margins, there are many factors that limit pyrite formation, mainly including availability of organic carbon which can be utilized for sulfate reduction, supply of sulfate from overlying seawater, accumulation of detrital iron-bearing minerals, and reactivity of iron-bearing minerals towards dissolved sulfide (e.g., Berner, 1970; Canfield, 1989; Aplin et al., 1993; Kao et al., 2004; Larrasoaña et al., 2007). Considering that Hydrate Ridge is located in an open ocean with deep water and normal salinity since the late Pliocene (< 2.6 Ma) (Shipboard Scientific Party, 2003a; Chevallier et al., 2006), the depositional and diagenetic system is completely open with respect to sulfate and thus sulfate reduction should not be diffusion limited (e.g., Jørgensen, 1979; Jørgensen et al., 2004). Also, because the organic carbon concentrations are relatively uniform (1.16 ± 0.36 wt%) at Sites 1245 and 1252 (Shipboard Scientific Party, 2003b, 2003c; Teichert and Bohrmann, 2006) and high enough to sustain sulfate reduction and methanogenesis (Claypool et al., 2006), the production of dissolved sulfide ($\Sigma HS = H_2S + HS^- + S^{2-}$) is always present.

According to the reactivities of iron-bearing minerals towards dissolved sulfide, half-lives for the reductive dissolution of ferric (hydr)oxides and magnetite are confined in time-scales of hours and tens of days (e.g., 12.3 h for ferrihydrite, 10.9 h for lepidocrocite, 63 d for goethite, 182 d for hematite, and 72 d for magnetite), which are much shorter than those of iron-bearing silicates, whose half-lives are tens of thousands of years (e.g., 84530 yr for sheet silicates) (Canfield et al., 1992; Poulton et al., 2004). Highly reactive iron (Fe_{HR}) therefore includes Fe_A, Fe_D, and Fe_O, in addition to iron which has been transformed to pyrite (i.e., Fe_{HNO3}) ($Fe_{HR} = Fe_A + Fe_D + Fe_O + Fe_{HNO3}$), whereas Fe_{HF} largely belongs to poorly reactive and unreactive iron. At Sites 1245 and 1252, concentrations of Fe_T are mostly distributed in range between 4 and 5 wt% (4.37 ± 0.46 wt% at Site 1245; 4.92 ± 0.33 wt% at Site 1252) and, despite occasional fluctuations, ratios of Fe_{HR} to Fe_T are relatively homogeneous throughout the whole profiles (37.4 ± 3.3% at Site 1245; 40.5 ± 4.3% at Site 1252) (Figure 5), implying a long-term steady-state history for highly reactive iron accumulation. Moreover, due to relative abundant Fe_D and Fe_O (26.7 ± 4.5% of Fe_T) with Fe_{HNO3} (3.1 ± 2.7% of Fe_T) (Figure 5), there is quite enough highly reactive iron for pyritization and the availability of highly reactive iron should not limit pyrite formation. Especially, on average, Fe_O concentration (17.6% of Fe_T) is almost twice as high as Fe_D (9.1% of Fe_T) (Figure 5). Such significant enrichment of magnetite is due to volcanic and detrital origins (Larrasoaña et al., 2007), where the detrital magnetite likely derives from basalt and/or andesite of the Cascade Arc (e.g., Reidel and Tolan, 1992; Strong and Wolff, 2003; Dominguez and van der Voo, 2014). But for all this, compared to other iron species, Fe_{HNO3} makes up only a tiny proportion of Fe_T (2.27 ± 1.82% at Site 1245; 3.91 ± 3.26% at Site 1252) (Figure 5), indicating only very small amounts of highly reactive iron transformed into pyrite.

Accounting for the remaining 3 to 18% of Fe_T (Figure 5), Fe_A extraction shows that siderite occurs throughout the whole profiles of Sites 1245 and 1252. Siderite is typically formed below the depths where dissolved sulfide is existed (Figure 1), but actually it can also grow within the sulfate reduction zone, provided that available dissovled sulfide does not consume all ferrous iron released by iron reduction (e.g., Pye et al., 1990; Larrasoaña et al., 2007; Liu et al., 2023). This not only explains siderite occurred in the sulfate reduction zone, but also supports its enrichment associated with greigite and pyrrhotite (Figure 4B). This means that dissolved sulfide is not enough to drive metastable iron sulfide minerals to become completely pyritized (e.g., Kao et al., 2004; Novosel et al., 2005; Roberts and Weaver, 2005; Larrasoaña et al., 2007; Fu et al., 2008; Liu et al., 2023). Thus, the formation of pyrite at Sites 1245 and 1252 largely depends on whether dissolved sulfide is sufficient to be able to complete pyritization.

Based on earlier rock magnetic research at southern Hydrate Ridge, Larrasoaña et al. (2007) thought that greigite and pyrrhotite are formed in deep sediments where dissolved sulfide production is limited by low concentration gradients of methane near disseminated gas hydrate, so that pyritization is not driven to completion. They approved that incipient pyritization is caused by limited supply of dissolved sulfide, while argued that greigite and pyrrhotite have a late origin related to gas hydrate deposits. However, considering that gas hydrate is unevenly distributed in the sediment column, this explanation fails to explain why these two magnetic sulfide minerals occur continuously through the whole sediment interval of Unit IV at Site 1245 (Figure 3). Figure 6A shows that most concentrations of Fe_A are inversely correlated with those of Fe_{HNO3} (except for a few deviated samples in Unit III of Site 1252), suggesting the sources of iron between siderite and pyrite balance and complement each other. Similar relationship and origins of pyrite and siderite were also observed in the brackish and marine environments on the East China Sea inner shelf, but the quantitative bulk analyses of these two minerals were not carried out (Liu et al., 2023). In view of the steady-state input history of highly reactive iron described above, the relationship between Fe_A and Fe_{HNO3} further indicates that pyrite and siderite are two end-members representing distinctly different effects of sulfidization on highly reactive iron. From this, relative abundance of pyrite and siderite in highly reactive iron can be used as a proxy to evaluate the degree of sulfidization. In Figure 6B, the ratios of Fe_{HNO3}/Fe_{HR} and Fe_A/Fe_{HR} are cross-plotted and all data points fall into three areas,

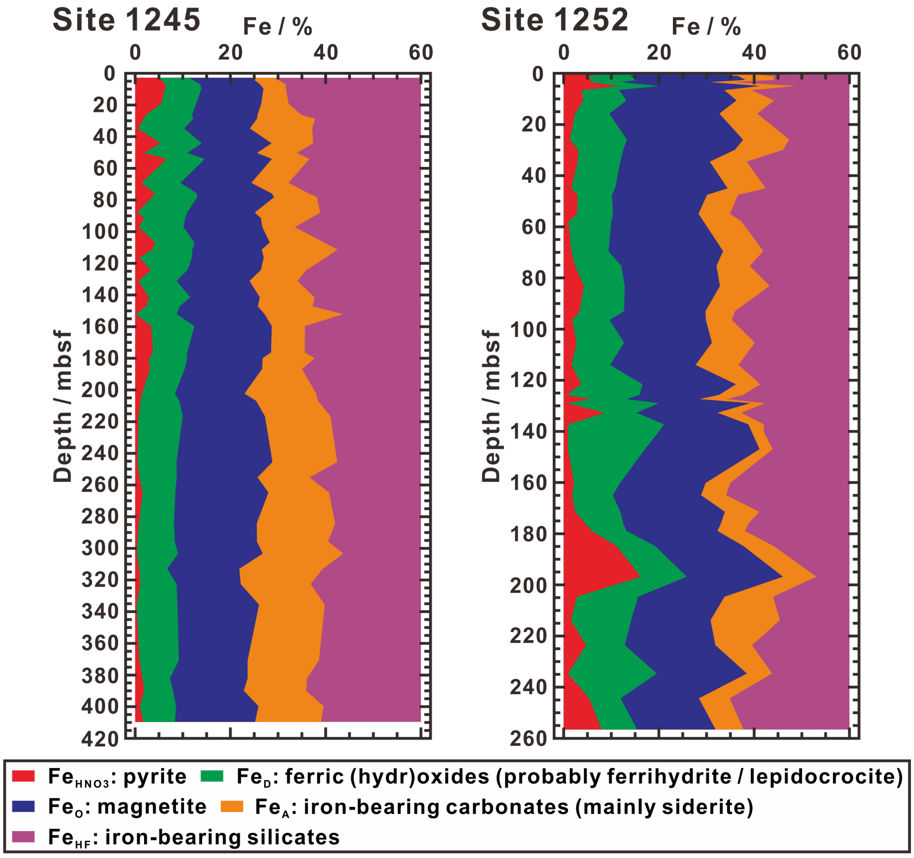

FIGURE 5
Profiles of relative concentrations of iron in extracted fractions (Fe_{HNO3}, Fe_D, Fe_O, Fe_A, and Fe_{HF}) at Sites 1245 and 1252. The species extracted from these fractions are also listed in legend. Note that the maximum value of the relative iron concentration on the x-axis is limited to 60%, and the remaining 40% of Fe_{HF} is not shown.

from which three degrees of sulfidization at Sites 1245 and 1252 can be classified as follows:

- Weak: The ratio of Fe_{HNO3}/Fe_{HR} is lower than 0.1 and the ratio of Fe_A/Fe_{HR} is higher than 0.3. Almost all of the samples with IRM@0.9T/χ ratios higher than 13.5 kA m^{-1} belong to this range, corresponding to the growth environment of greigite and/or pyrrhotite.
- Moderate: The ratio of Fe_{HNO3}/Fe_{HR} is lower than 0.1 and the ratio of Fe_A/Fe_{HR} is also lower than 0.3. In this case, samples contained greigite and/or pyrrhotite (IRM@0.9T/χ > 13.5 kA m^{-1}) tend to be rare or non-existent.
- Strong: The ratio of Fe_{HNO3}/Fe_{HR} is higher than 0.1 and the ratio of Fe_A/Fe_{HR} is lower than 0.3. Pyrite is the only sulfide mineral phase in this range.

According to this classification, downcore pattern of sulfidization degrees at Sites 1245 and 1252 are well identified in terms of both ratios of Fe_A/Fe_{HR} and Fe_{HNO3}/Fe_{HR} as shown in Figure 7. Based on a close association of siderite with greigite and/or pyrrhotite, IRM@0.9T/χ ratios are also used as a supplementary criterion to determine the weak degree of sulfidization. In the following text, we will combine sulfur isotope geochemistry and provide a new perspective to explain the downcore variation of sulfidization degrees.

5.3 Sulfur isotope variation of pyrite and its relation to non-steady-state scenarios

Sulfur isotopic compositions of S_{CR} are listed in Table 1 and show a complex distribution with depth, ranging from -38.3 to +13.0‰ at Site 1245 and from -42.4 to +16.8‰ at Site 1252 (Figure 7). As described above, pyrite is most likely the only mineral phase extracted as S_{CR}, the $\delta^{34}S$ values of S_{CR} are therefore equivalent to the sulfur isotopic compositions of authigenic pyrite at each sampling depth.

During the early diagenesis, it is normally considered that dissolved sulfide becomes more enriched in ^{34}S as pore water sulfate is consumed with burial depth, and reaches maximum $\delta^{34}S$ values in the SMT zone (e.g., Aharon and Fu, 2000; Jørgensen et al., 2004; Borowski, 2006). Due to an insignificant sulfur isotope fractionation (ca. 1‰) involved in pyritization, pyrite should record the sulfur isotope ratio of its source dissolved sulfide (e.g., Price and Shieh, 1979; Wilkin and Barnes, 1996; Böttcher et al., 1998). In this case, sulfur isotopes of dissolved sulfide at each depth enter pyrite so that pyrite gradually becomes more enriched in ^{34}S with progressive burial, and thus the isotopically heaviest pyrite occurs in the SMT zone (e.g., Jørgensen, 1979; Jørgensen et al., 2004; Borowski et al., 2013; Lin et al., 2016). Under steady-state conditions of pore water profiles (e.g., a constant SMT depth below the seafloor), sulfur isotopic record in pyrite will be unchanged with depth once below the SMT zone. It denotes that pyrite should have uniform or small changed $\delta^{34}S$ values in the sediment column below the present-day SMT zone if steady-state conditions are kept. Throughout the whole $\delta^{34}S$ profiles of pyrite, the smallest range in variability of $\delta^{34}S$ is only reached in Unit IV of Site 1245 (-24.0 ± 6.4‰) (Figure 7). So it is reasonable to assume that steady-state conditions of pore water profiles were sustained during its depositional history. Instead, the magnitude of pyrite $\delta^{34}S$ change (-42.4 ~ +16.8‰) occurred in other lithostratigraphic (sub) units of Sites 1245 and 1252 (Figure 7) indicates that non-steady-state scenarios must have happened.

Significantly ^{34}S-depleted pyrite (-30.1 ~ -42.4‰) occur repeatedly through the sediment columns (Figure 7), which yields isotopic fractionation larger than 50‰ relative to present-day seawater sulfate (ca. +21‰; Rees et al. (1978)). These extremely low $\delta^{34}S$ values presumably result from disproportionation of sulfur intermediates (e.g., S^0, SO_3^{2-}, and $S_2O_3^{2-}$) produced in a repeated cycle of sulfide oxidation and sulfate reduction (e.g., Canfield and Thamdrup, 1994; Böttcher et al., 2001). Isotopically light pyrite in these sedimentary layers is most likely formed in the uppermost sulfate reduction zone in the beginning of sulfate reduction and may be associated with infaunal activity, seeing that bioturbation signs are frequently visible in the sediment cores (for detail about bioturbation signs, see Shipboard Scientific Party (2003b, 2003c)). So we inferred that these large depletions in ^{34}S form the background level or baseline of pyrite $\delta^{34}S$ from which heavy sulfur isotope accumulates gradually as the sulfate reduction progresses with burial depth in the sulfate reduction zone (e.g., Jørgensen, 1979; Borowski et al., 2013; Lin et al., 2016). The sulfur isotopic records which are still being preserved to this day demonstrate that non-steady-state scenarios of pore water profiles must be prevalent by which the enrichment of ^{34}S in pyrite is interrupted.

Liu X. et al. (2019) presented an obvious pyrite sulfur isotope variations (-38.2 ~ +15.0‰) from the inner shelf sediments of the East China Sea, which show a positive relationship with changes in sedimentation rate. Although this $\delta^{34}S$ range is generally consistent with our results, the depositional conditions are quite different. The sedimentation rates of the inner shelf (up to 2.3 cm a^{-1}) are almost one to two orders of magnitude higher than those of the lower continental slope in this study. Therefore, in our study area, it is impossible to form a “restricted” diagenetic system and the resulting isotopically heavy pyrite due to rapid deposition as in the inner shelf environments.

Borowski et al. (2013) took authigenic sulfide minerals from the Blake Ridge (Sites 994 and 995 on ODP Leg 164 and piston core 11–8) as example and showed that, within or near the SMT zone, these sulfide minerals are enriched in ^{34}S by at least 20‰ on average compared to background $\delta^{34}S$ levels of -40 to -50‰. They further proposed that larger ^{34}S enrichment needs larger amount of sulfide minerals precipitated in the SMT zone and positive values of ^{34}S enrichment require non-steady-state conditions where the SMT zone stagnates in the same sedimentary layer for a considerable length of geologic time. In this study, we also found that $\delta^{34}S$ values of pyrite in the present-day SMT zone are ca. -20‰ (Figure 7). We therefore adopted -20‰ (i.e., 20‰ higher than the background level of ca. -40‰) and 0‰ as two $\delta^{34}S$ thresholds to evaluate the magnitude of ^{34}S enrichment in pyrite. Depth profiles of this sulfur isotopic identification in the sediment columns of Sites 1245 and 1252 are shown in Figure 7.

Pyrite with $\delta^{34}S$ values higher than -20‰ may have another origin related to a shallower SMT zone where AOM arises close to the seafloor. In this case, it is to be expected that, by overlapping organoclastic sulfate reduction (OSR) with AOM, coupled sulfate reduction rate tends to be anomalously higher than decoupled one. Experimental studies and field observations both indicated that sulfur isotope fractionation factor between sulfate and dissolved sulfide is inversely dependent on the rate of sulfate reduction (e.g., Harrison and Thode, 1958; Kemp and Thode, 1968; Goldhaber and Kaplan, 1975). Aharon and Fu (2000) estimated that rates of sulfate reduction at cold seeps in the Gulf of Mexico (0.27 ~ 2.51 μmol SO_4^{2-} cm^{-3} d^{-1}) are up to 600 times higher than those at non-seep reference sites, while the sulfur isotopic fractionation factors (α = 1.009 ~ 1.018) are substantially lower than the latter (α = 1.027). Measured rates of sulfate reduction at the summit of southern Hydrate Ridge were 0.12 to 5 μmol SO_4^{2-} cm^{-3} d^{-1} (Boetius et al., 2000; Nauhaus et al., 2002; Treude et al., 2003), which are of the same order of magnitude as those at cold seeps in the Gulf of Mexico. The rapid sulfate reduction at the summit is due to OSR coupled with AOM near the seafloor, where the shallow SMT zone is being fueled by active seeping of gaseous methane. Thus, if similar phenomenon suddenly happened (i.e., uplift of the SMT zone) in the depositional history of Sites 1245 and 1252, the decrease in sulfur isotope fractionation effect would generate higher pyrite $\delta^{34}S$ values (≥ -20‰ or even ≥ 0‰) than those occurred under the deep SMT conditions.

The third cause of isotopically heavier pyrite may come from non-steady-state depositional events. When diagenetic front moves upward at a similar rate to sedimentation rate, isotopically light pyrite must be accumulated in the sedimentary layer before it is buried in the SMT zone. This means that the enrichment of ^{34}S in pyrite generated in the SMT zone must be mixed with the large pool of the ^{34}S-depleted pyrite produced earlier in the upper sulfate reduction zone, resulting in a weakening of the magnitude of ^{34}S enrichment in bulk pyrite. However, if a massive deposition suddenly occurs, upward shift of diagenetic front will temporarily lag behind it. It may take hundreds of years to wipe out the original pore water signature and to develop new pore water profiles (e.g., Zabel and Schulz, 2001; Hensen et al., 2003). This time period of pore water update is still very short relative to the history of sulfide formation. So the SMT zone will rapidly lift into the freshly deposited sediment interval where little pyrite has been formed before (considering that pyrite cannot be retained during transport in the oxygenated seawater). In this case, the isotopically heavy signal of AOM-derived pyrite can be preserved intact, without the effects of the earlier ^{32}S depletion. The extremely positive values of pyrite $\delta^{34}S$ (≥ 0‰) therefore occur in the SMT zone developed after the massive deposition event.

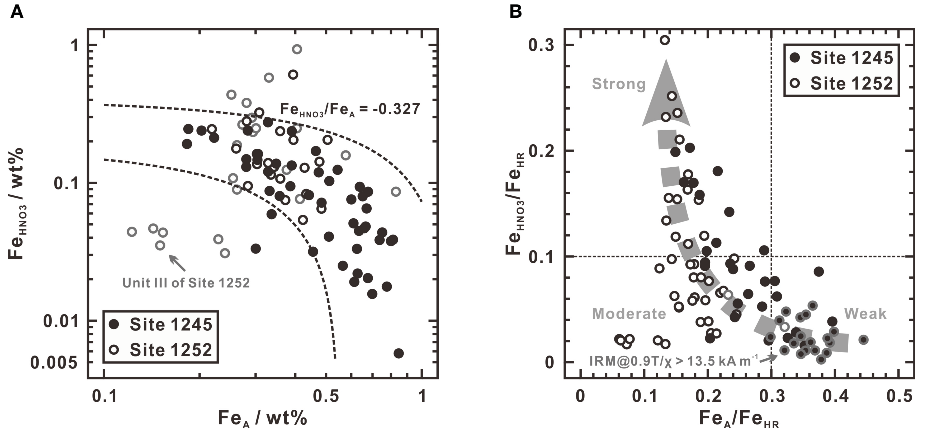

FIGURE 6
Plots of Fe_A versus Fe_{HNO3} **(A)** and Fe_A/Fe_{HR} versus Fe_{HNO3}/Fe_{HR} **(B)** at Sites 1245 and 1252. In **(A)**, most data points show an inversely linear relation with a slope of -0.327. Samples from Unit III of Site 1252 are outlined in gray. Note that the deviated samples are largely from them. In **(B)**, Fe_{HR} is calculated as the sum of Fe_A, Fe_D, Fe_O, and Fe_{HNO3}. The gray dashed arrow indicates an enhanced trend of sulfidization degrees constrained by ratios of Fe_A/Fe_{HR} and Fe_{HNO3}/Fe_{HR}. The gray outlined circles represent the samples with IRM@0.9T/χ ratios higher than 13.5 kA m^{-1}.

5.4 Development of conceptual steady-state and non-steady-state scenarios

According to biostratigraphic ages (Shipboard Scientific Party, 2003b, 2003c; Watanabe, 2006), the interpolated sedimentation rates at Site 1245 and 1252 can be sorted into seven levels: 1 ~ 5, 10 ~ 15, 20 ~ 25, 45 ~ 50, 50 ~ 55, 60 ~ 65, and ca. 290 cm ka^{-1} (Figure 7). Such variable sedimentation rates provide inspiration for different non-steady-state scenarios developed here. In addition, previous research at Hydrate Ridge showed that stability of underlying gas hydrate was disrupted episodically (e.g., Tréhu et al., 1999; Teichert et al., 2003; Bangs et al., 2005). Any released methane would increase upward methane flux so that the SMT zone would move upward to a shallower depth. Therefore, in dynamic continental margin sediments, the most likely causes of non-steady-state scenarios are variations in sedimentation rate and methane flux.

Based on the early diagenetic reactions outlined in Figure 1 and above discussion, we proposed seven conceptual scenarios to explain the depth variations in sulfidization degree and pyrite $\delta^{34}S$ value. We began with two steady-state scenarios based on different sedimentation rates (Scenarios 1 and 2), from which the following non-steady-state scenarios were derived. These non-steady-state scenarios are classified into two categories; those based on sedimentation rate variation (Scenarios 3 to 5) and those based on methane flux variation (Scenarios 6 and 7). All the scenarios are based on three assumptions operative at Hydrate Ridge throughout its depositional history: (1) the bottom seawater remains oxic; (2) the availabilities of organic carbon, seawater sulfate, and highly reactive iron are sufficient for pyritization and their supplies vary little with time; and (3) the injection of oxygen into suboxic and anoxic sediments by bioturbation often occurs near the seafloor that creates the background $\delta^{34}S$ levels of pyrite (ca. -40‰). Under these conditions, pyrite and siderite accumulate in the same geochemical zone but in different proportions. All these scenarios begin with a steady-state situation where the equilibrated geochemical zonation and mineralization has been established.

5.4.1 Scenarios 1 and 2 (steady-state conditions with different sedimentation rates)

In Scenario 1, rapid and constant deposition occurs (Figure 8). High sedimentation rate (e.g., > 60 cm ka^{-1}) not only compresses geochemical zones but also causes incomplete pyritization. This means that iron-bearing minerals do not have enough time to react with dissolved sulfide to form pyrite. In this case, only a small fraction of reactive iron can form pyrite, but abundant siderite accumulates in the sulfate reduction zone. With continued sediment burial, diagenetic front will move upward and this geochemical pattern of pyrite and siderite will be recorded in the sediment column, which represents a product of weak degree of sulfidization. Metastable precursors to pyrite, i.e. gregite and/or pyrrhotite, can also be preserved due to their limited exposure to dissolved sulfide. Although ^{34}S-enriched dissolved sulfide is produced in the SMT zone, it may have little chance to neutralize the ^{34}S-depleted pyrite accumulated earlier due to rapid sweeping of the SMT zone upward over the upper sulfate reduction zone. From this, $\delta^{34}S$ values of pyrite almost cannot be higher than -20‰.

Scenario 2 shows slow and constant deposition that results in an opposite geochemical pattern of pyrite and siderite (Figure 8). Low sedimentation rate (e.g., < 25 cm ka^{-1}) causes geochemical zones to expand in thickness so that the front of pyritization occurs at deeper depths. This gives enough time for complete pyritization in the sulfate reduction zone while only a small amount of siderite is formed, showing a product of strong degree of sulfidization. With progressive burial, dissolved sulfide enriched in ^{34}S will gradually accumulate in pyrite, producing moderate or higher values of $\delta^{34}S$ (≥ -20‰).

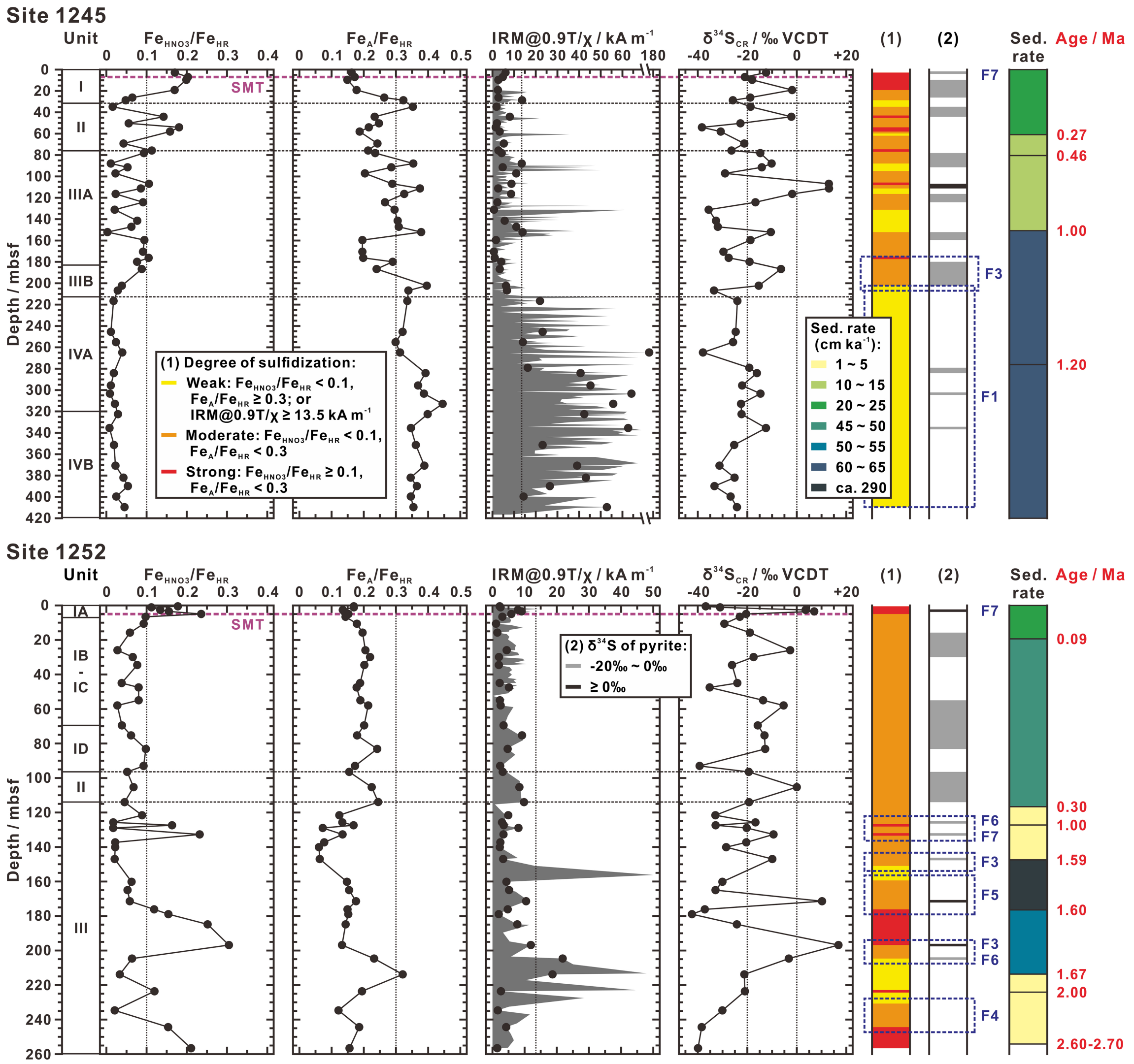

FIGURE 7
Depth distributions of degree of sulfidization and sulfur isotopic composition of pyrite at Sites 1245 and 1252. The profiles include ratios of Fe$_{HNO3}$/Fe$_{HR}$, Fe$_A$/Fe$_{HR}$, IRM@0.9T/χ, and δ^{34}S values of S$_{CR}$ (δ^{34}S$_{CR}$). Classification of degree of sulfidization shown in column (1) is determined according to the criterion derived from Figure 6B. The δ^{34}S values of S$_{CR}$ are equal to the sulfur isotopic compositions of pyrite, where values higher than -20‰ and 0‰ are identified in column (2). Sedimentation rate (sed. rate) is interpolated in terms of biostratigraphic ages labeled as red numbers. Blue dotted rectangles and labels (F1 ~ F7) indicate the positions where the features of conceptual scenarios are recognized in the sediment columns. Locations of the present-day SMT zones (purple dashed horizons) are given by Shipboard Scientific Party (2003b, 2003c). The column Unit represents lithostratigraphic (sub) unit.

5.4.2 Scenarios 3 to 5 (non-steady-state events with changing sedimentation rate)

By integrating Scenarios 1 and 2, we deduced Scenarios 3 to 5 by changing sedimentation rates (Figure 9). For Scenario 3, when sedimentation rate decreases, geochemical pattern of pyrite and siderite will change from the product of weak degree of sulfidization formed by rapid deposition into a stronger one upward. In this case, part of siderite formed earlier will be pyritized so that a product of moderate degree of sulfidization occurs. At the same time, moderate or higher values of pyrite δ^{34}S (≥ -20‰) should be present after weak sulfidization ends. In Scenario 4, the opposite effect occurs when sedimentation rate increases during which weakened sulfidization tends to decrease δ^{34}S values in pyrite (< -20‰).

Scenarios 3 and 4 are more complicated than Scenarios 1 and 2, and thus may approach actual occurrences in nature. However, they are still far from sufficient for more complex situations. Scenario 5 considers the occurrence of a sudden, massive depositional event that dumps thick sediments on the seafloor, thus affecting the continued diagenesis. Because this event can be treated as an extreme case of sedimentation rate increase, its variation in sulfidization degree and pyrite δ^{34}S value are both similar to those of Scenario 4. But, as described above, due to its occurrence much faster than the upward shift of diagenetic front, pore water profiles will later evolve in the freshly deposited sediment column and pyrite formed in the new SMT zone would be extremely enriched in ^{34}S (≥ 0‰).

5.4.3 Scenarios 6 and 7 (non-steady-state events with changing methane flux)

Scenarios 6 and 7 show non-steady-state conditions as methane flux varies (Figure 10). In Scenario 6, the upward shift of SMT zone triggered by a rise in methane flux will interrupt the former steady-state conditions of weak sulfidization and move the front of pyritization higher in the sediment column toward the seafloor. As elaborated above, overlapping OSR with AOM will produce extremely high rate of sulfate reduction and a small sulfur isotope fractionation between sulfate and dissolved sulfide. In this case, pyritization tends to completion upward and the isotopically light pyrite formed earlier would be erased by more ^{34}S-enriched pyrite newly formed. After this, if the SMT zone maintains at a shallow depth, the product of high degree of sulfidization and high values of δ^{34}S (≥ -20‰ or even > 0‰) will be continued in the sediment column.

Scenario 7 outlines the geochemical response as lower methane flux causes deepening of the SMT zone. To examine whether the δ^{34}S signature of the shallow SMT zone could be preserved, we chose to begin Scenario 7 just after the end of Scenario 6. Descending SMT zone means lowing the rate of sulfate reduction, which will favor siderite formation and increase sulfur isotope fractionation between sulfate and dissolved sulfide. Thus, the sulfidization degree becomes weaker and high ^{34}S-enrichment in pyrite generated in the former shallow SMT zone may be partially erased by the ^{34}S-depleted pyrite formed after the downward SMT movement.

5.5 Comparison of scenario predictions and real observations

Each developed scenario has a specific geochemical feature of the variation in sulfidization degree and pyrite δ^{34}S value. We searched similar features in the sediment columns of Sites 1245 and 1252. Once the features were found, we ascribed them to the certain scenario and then the non-steady-state event behind it was tested by the real observations (e.g., sedimentary, mineralogy, and tectonic evidences).

5.5.1 Feature of Scenario 1

The feature of Scenario 1 is uniformly weak sulfidization degree and low value of pyrite δ^{34}S (< -20‰) (Figure 8). It is recognized throughout Unit IV of Site 1245 despite sporadic pyrite δ^{34}S values slightly higher than -20‰ (Figure 7). Based on Scenario 1, sedimentation rate should be high, which is in good agreement with the observed sedimentation rate (61 ~ 63 cm ka^{-1}) before ca. 1.00 Ma.

5.5.2 Feature of Scenario 3

In Scenario 3, the degree of sulfidization increases upward in the sedimentary record and higher value of pyrite δ^{34}S (≥ -20‰) becomes more apparent (Figure 9). These properties occur within three depth intervals: ca. 170 ~ 210 mbsf of Site 1245 (Interval a), ca. 195 ~ 210 mbsf of Site 1252 (Interval b), and ca. 145 ~ 155 mbsf of Site 1252 (Interval c) (Figure 7). In Intervals a and b, the feature of Scenario 3 is perfectly met. In Interval c, the sulfidization degree increases upward and the signature of higher pyrite δ^{34}S (≥ -20‰) is identified, which is consistent with the feature, though the final degree of sulfidization does not reach the strong level. From Scenario 3, sedimentation rate decreases. This prediction can be verified by the sedimentation rate changes of Interval a (from 61 ~ 63 cm ka^{-1} to 10 ~ 23 cm ka^{-1} at ca. 1.00 Ma) and Interval c (from ca. 290 cm ka^{-1} to 1 ~ 5 cm ka^{-1} at ca. 1.59 Ma). In Interval b, no corresponding change can be observed in sedimentation rate, but smear slide analysis indicated that at least two sedimentary layers contain over 10% of glauconite (197.25 and 178.60 mbsf; see Shipboard Scientific Party (2003c)), which may be supportive of a low sedimentation rate and perhaps a lower-energy environment at that time (e.g., Leeder, 1999).

5.5.3 Feature of Scenario 4

In contrast to Scenario 3, Scenario 4 shows an upward decrease in sulfidization degree and δ^{34}S value of pyrite (< -20‰) (Figure 9). Similar variation in sulfidization degree is recognized near the bottom of the sampling depth at Site 1252 (ca. 225 ~ 250 mbsf), though the signature of higher pyrite δ^{34}S (≥ -20‰) is not identified (Figure 7). Scenario 4 suggests an increase in sedimentation rate. This prediction is consistent with the observed increasing sedimentation rate from 1 ~ 5 cm ka^{-1} to ca. 53 cm ka^{-1} at ca. 1.67 Ma. The signature of higher pyrite δ^{34}S (≥ -20‰) may be missed by low sampling resolution.

5.5.4 Feature of Scenario 5

The feature of Scenario 5 is not much different from that of Scenario 4, but the former has an extremely ^{34}S-enriched record in pyrite (≥ 0‰) (Figure 9). In Unit III of Site 1252, sandwiched between two features of Scenarios 3, the sequence of sulfidization degree (ca. 155 ~ 180 mbsf) and the signature of isotopically heavy pyrite (≥ 0‰) are both coherent with the feature of Scenario 5 (Figure 7). As predicated by Scenario 5, a sudden, massive deposition process (ca. 290 cm ka^{-1}) did occur at ca. 1.60 Ma.

5.5.5 Features of Scenarios 6 and 7

Scenario 6 presents a similar sulfidization sequence as the feature of Scenario 3 (i.e., upward increasing sulfidization degree) except that higher values of pyrite δ^{34}S (≥ 0‰) may occur (Figures 9 and 10). As mentioned above, Interval b (ca. 195 ~ 210 mbsf of Site 1252) has been recognized as the feature of Scenario 3. Nevertheless, an extremely ^{34}S-enriched isotopic signature of pyrite (+16.84‰) occurs at 196.80 mbsf (Figure 7). It probably results from Scenario 6 that increasing methane flux forced the SMT zone higher in the sediment column toward the seafloor. This SMT zone uplift may be almost simultaneous with the decrease in sedimentation rate, so that their changes in sulfidization degree wholly overlap. Visual core description exhibited multiple carbonate-cemented layers between ca. 179 and 192 mbsf (Shipboard Scientific Party, 2003c), which provides adequate support for an intensive AOM arising in a shallow SMT zone.

Frequent fluctuations in sulfidization degree and pyrite δ^{34}S value occur near the top of Unit III at Site 1252 (ca. 115 ~ 140 mbsf)

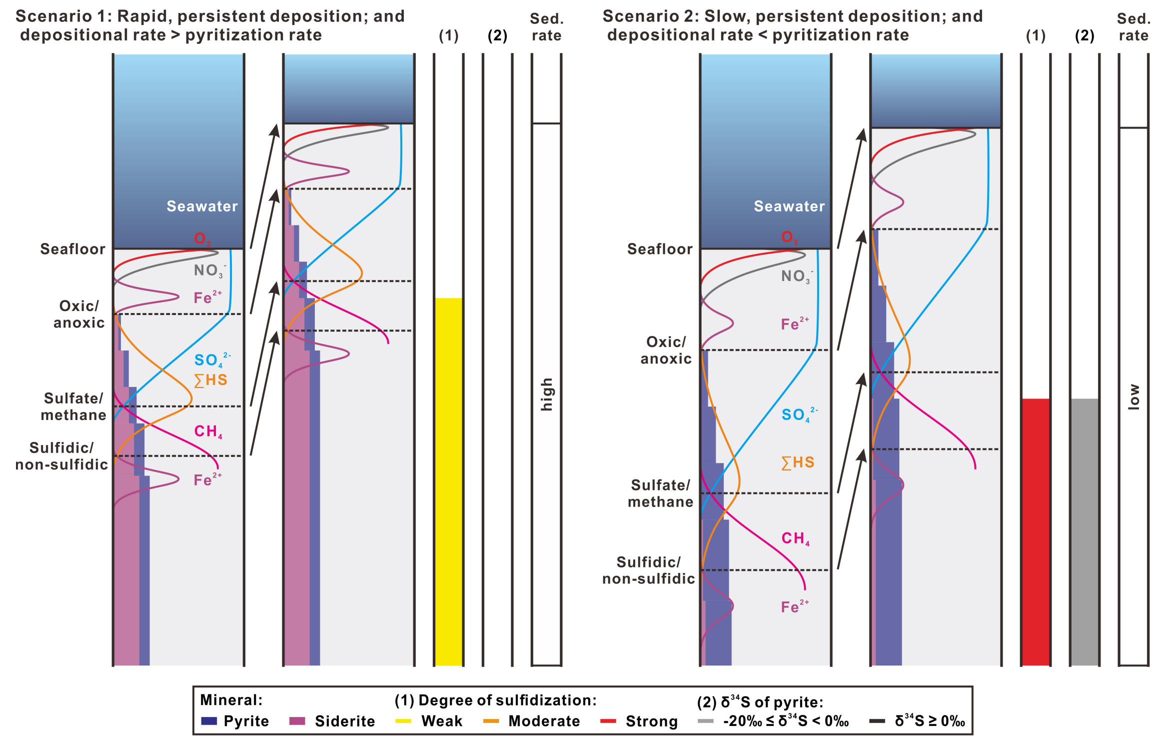

FIGURE 8
Schematic diagrams of steady-state Scenarios 1 and 2 based on different sedimentation rates (sed. rate) and their predicted features in degree of sulfidization (1) and sulfur isotopic composition of pyrite (2). Colored pore water curves are consistent with Figure 1. Solid and dotted horizons mark the seafloor and the redox-driven geochemical boundaries. Accumulations of pyrite and siderite are indicated qualitatively by widths of blue and purple bars, from which degrees of sulfidization are inferred. For each scenario, the first panel shows initial conditions and the following panels represent a time step of unspecified length with new deposition. Arrows indicate shifts of the seafloor and boundaries after the time step.

(Figure 7). From ca. 1.00 to 0.30 Ma, Site 1252 experienced a very slow deposition (1 ~ 5 cm ka^{-1}) or an intermittent depositional interruption, as supported by at least two glauconite-rich (40% in smear slide) layers at 116.03 and 113.82 mbsf (Shipboard Scientific Party, 2003c). This implies that the impact of the sedimentation rate variation can be excluded. From Scenarios 6 and 7, we knew that the signatures of sulfidization degree and pyrite $\delta^{34}S$ value formed in the shallow SMT zone can be partially saved even if the SMT zone falls soon (Figure 10). Through repeated rise and fall of SMT zone, a rhythmic pattern of different sulfidization degrees and pyrite $\delta^{34}S$ values would be finally present in the sedimentary column. This feature may be consistent with that observed at Site 1252 (Figure 7). Visual core description also verified that abundant carbonate precipitates as the diagenetic indicator of AOM are clustered between 121 and 127 mbsf (Shipboard Scientific Party, 2003c). Based on the regional tectonic history evolved by Chevallier et al. (2006), Anticline B started to be uplifted relative to the core of Hydrate Ridge soon after 1.0 Ma and has stopped since 0.3 Ma. It is reasonable to believe that the uplift of Anticline B led to decomposition of underlying gas hydrate, creating a similar pressure effect as a drop in sea level. The repeated changes in sulfidization degree and pyrite $\delta^{34}S$ value may denote that the uplift of Anticline B is discontinuous, resulting in an episodic methane release.

Besides above, it is noteworthy that, compared to -20‰ of ^{34}S-enrichment in the present-day SMT zones, higher $\delta^{34}S$ values of pyrite occur at above depths, i.e. -12.43‰ at 2.80 mbsf of Site 1245, + 3.57‰ at 2.60 mbsf of Site 1252, and +7.05‰ at 3.45 mbsf of Site 1252 (Figure 7). Considering the AOM-dominated pyrite tends to enrich ^{34}S, it may indicate that the SMT zones once existed at a shallower depth, and before long fell to the present-day levels. This is well suited to the design of Scenario 7 (Figure 10). The ^{34}S-enriched isotope signatures left by the shallow ancient SMT zone have been saved after the downward SMT movement. Especially at Site 1252, two remained positive $\delta^{34}S$ values of pyrite perhaps imply that the former SMT zone was stagnated at these sedimentary layers for a relatively length of geologic time. According to the recognition from Borowski et al. (2013), these two layers may represent the stratigraphic locations of “fossil” or “paleo” SMT zones. Estimated by the interpolated sedimentation rates, these positive $\delta^{34}S$ layers deposited at ca. 16 to 12 ka, so that they must be formed after the Last Glacial Maximum 18 ka ago. Bangs et al. (2005) thought that an increase in bottom seawater temperature promoted decomposition of gas hydrate during the recent postglacial period. The released methane would shift the SMT zone into a shallow depth. That should be the reason for positive excursions of pyrite $\delta^{34}S$. Since then, the underlying gas hydrate kept stable and thereafter the decreasing contribution of the released methane shifted the SMT zone downward.

5.5.6 Indistinguishable features

In addition to above features, some variations in sulfidization degree and pyrite $\delta^{34}S$ value cannot yet be clearly attributed to the certain scenario, which are mainly distributed in Units I to III of Site

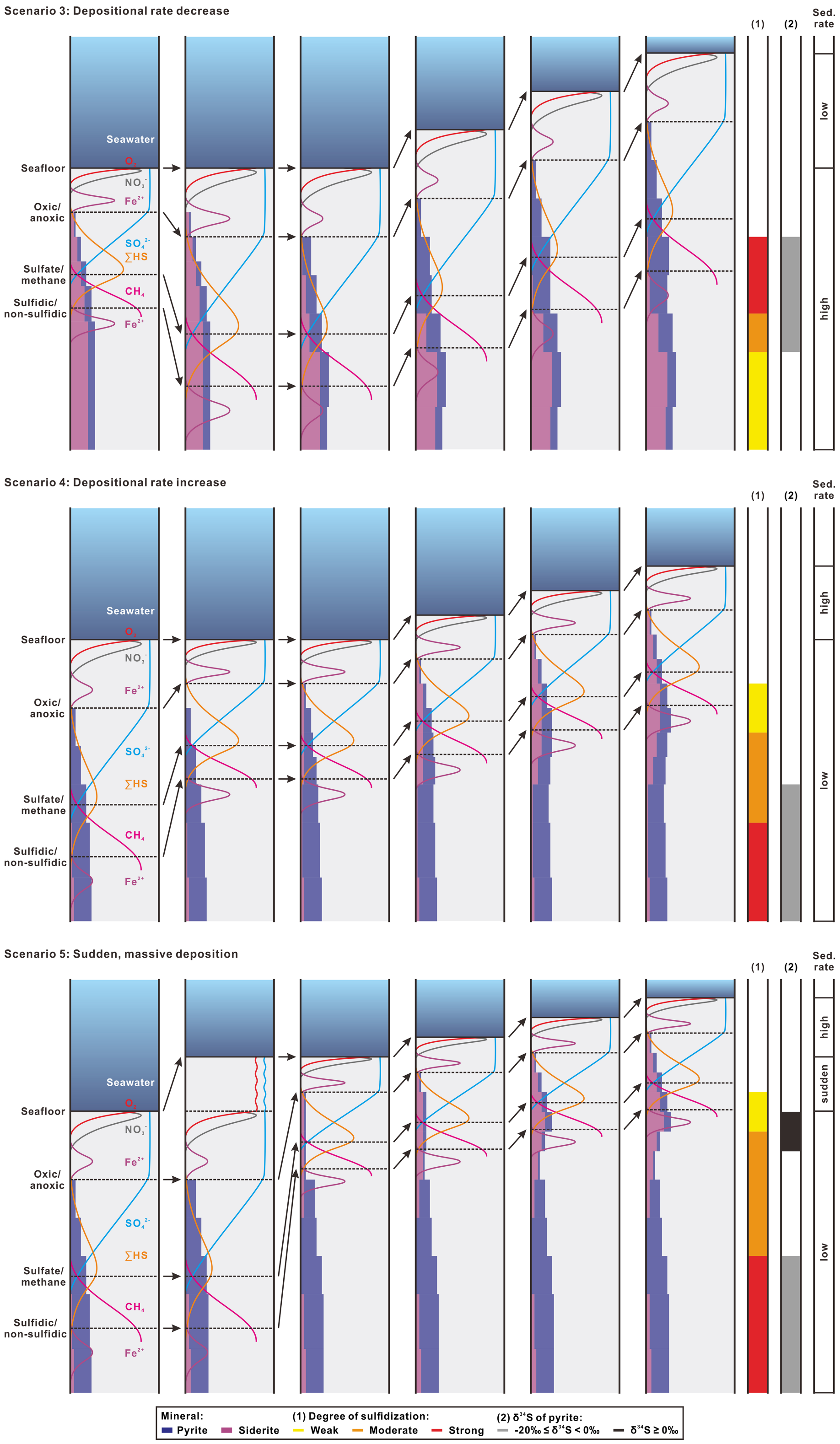

FIGURE 9
Schematic diagrams of non-steady-state Scenarios 3 to 5 deduced by changing sedimentation rate (sed. rate) and their predicted features in degree of sulfidization (1) and sulfur isotopic composition of pyrite (2). Refer to the caption of Figure 8 for an explanation of figure format and symbols. Note that part of the siderite formed earlier can be pyritized if sulfidized, but not vice versa.

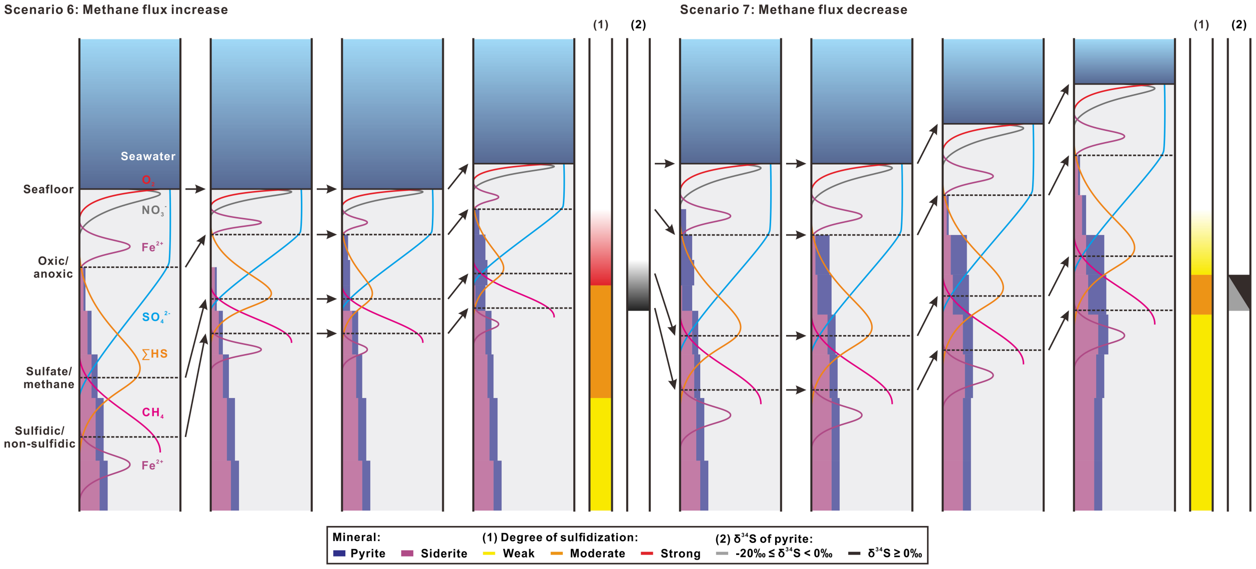

FIGURE 10
Schematic diagrams of non-steady-state Scenarios 6 and 7 that change methane flux and their predicted features in degree of sulfidization (1) and sulfur isotopic composition of pyrite (2). Refer to the caption of Figure 8 for an explanation of figure format and symbols. For each scenario, change in methane flux begins from the second panel.

1245 and in Units I and II of Site 1252 (Figure 7). In these sediment intervals, although the interpolated sedimentation rate tends to be stable, turbidity currents, debris flows, and notable ash layers frequently occur in a short time scale (Shipboard Scientific Party, 2003b, 2003c). At the same time, gas hydrate decomposition and methane release at the Hydrate Ridge were present episodically during the past 1.00 Ma (e.g., Tréhu et al., 1999; Teichert et al., 2003; Bangs et al., 2005). Thus, we thought that the highly cyclic changes in sulfidization degree and pyrite $\delta^{34}S$ value at Site 1245 perhaps result from repeated small-scaled depositional events, or methane flux fluctuation, and combination of them. Similar situation would also prevail at Site 1252, while the continued moderate degree of sulfidization may be largely constrained by the medium sedimentation rate (ca. 46 cm ka^{-1}).

6 Conclusions

This study investigated how and to what extent the non-steady-state depositional and diagenetic changes affect the distributions of iron-bearing mineral phase and sulfur isotopic composition of pyrite in the sediment columns. For this purpose, a modified sequential extraction procedure for iron was applied to two sediment sequences of Sites 1245 and 1252 recovered during ODP Leg 204 at southern Hydrate Ridge, Cascadia Margin, from which five iron species were characterized: (1) Fe_A: iron-bearing carbonates, mainly siderite; (2) Fe_D: ferric (hydr)oxides, probably ferrihydrite and/or lepidocrocite; (3) Fe_O: magnetite; (4) Fe_{HF}: iron-bearing silicates; and (5) Fe_{HNO3}: pyrite. Two reduced sulfur species, S_{AV} and S_{CR}, were also extracted and recognized as greigite and/or pyrrhotite and pyrite, respectively, despite the concentration levels of S_{AV} far lower than those of S_{CR}.

Downcore distributions of Fe_{HR} are almost invariable relative to Fe_T, suggesting a long-term steady-state history for highly reactive iron accumulation. The availability of organic carbon, seawater sulfate, and highly reactive iron are all not the limitation factors for pyritization. Formation of pyrite should be controlled by the limited supply of dissolved sulfide relative to abundant availability of highly reactive iron. The inverse relationship between Fe_A and Fe_{HNO3} further indicates that effects of sulfidization can be reflected by the proportion of pyrite and siderite. Therefore, ratios of Fe_A/Fe_{HR} and Fe_{HNO3}/Fe_{HR} were chosen as a proxy to evaluate the degree of sulfidization and three levels were classified: weak ($Fe_{HNO3}/Fe_{HR} < 0.1$, $Fe_A/Fe_{HR} \ge 0.3$), moderate ($Fe_{HNO3}/Fe_{HR} < 0.1$, $Fe_A/Fe_{HR} < 0.3$), and strong ($Fe_{HNO3}/Fe_{HR} \ge 0.1$, $Fe_A/Fe_{HR} < 0.3$).

Sulfur isotopic compositions of pyrite are very inhomogeneous with depth (-42.4 ~ +16.8‰), except for Unit IV of Site 1245 with relatively small variability (-24.0 ± 6.4‰). These results indicate that the steady-state conditions were sustained during deposition of Unit IV at Site 1245 but other lithostratigraphic (sub)units show frequent non-steady-state signatures. These non-steady-state events interrupted the enrichment of ^{34}S in pyrite in the sulfate reduction zone, and left the background $\delta^{34}S$ levels of -30.1 to -42.4‰. We suggested that pyrite with $\delta^{34}S$ values higher than -20‰ may have two non-steady-state origins: one is an upward shift of SMT zone close to the seafloor where overlapping OSR with AOM decreases sulfur fractionation effect; the other one is a sudden, massive deposition that lifts the SMT zone rapidly into the new deposited sediment column without loading ^{34}S-depleted background pyrite.

From early diagenetic pathways of iron and sulfur, we proposed two categories of conceptual non-steady-state scenarios based on variations in sedimentation rate and methane flux. Specific features of the variations in sulfidization degree and pyrite $\delta^{34}S$ value were predicted by every scenario and then searched in the measured results. The non-steady-state processes behind the matching scenarios were compared to the real observations (e.g., evidence from sedimentation rate, AOM-derived carbonates, and tectonic activity). Our conceptual scenarios well explained the main variations in sulfidization effect and pyrite $\delta^{34}S$ value through both Unit III of Site 1252 and (Sub)Units IV to IIIB of Site 1245 as being the result of the non-steady-state depositional events, and further provided some hints about heretofore unknown episodes of methane release. We believed that these conceptual scenarios may contribute to reconstruction of non-steady-state processes in other research areas.

Data availability statement

The original contributions presented in the study are included in the article/supplementary material. Further inquiries can be directed to the corresponding author.

Author contributions

CL: Conceptualization, Funding acquisition, Investigation, Methodology, Writing – original draft, Writing – review & editing. SJ: Conceptualization, Resources, Supervision, Writing – review & editing. XS: Conceptualization, Resources, Supervision, Writing – review & editing. XB: Writing – original draft, Writing – review & editing. HD: Investigation, Methodology, Resources, Writing – review & editing. DL: Methodology, Resources, Writing – review & editing. TY: Resources, Writing – review & editing.

Funding

The author(s) declare financial support was received for the research, authorship, and/or publication of this article. This research was financially supported by the National Natural Science Foundation of China (Grant No. 41806059).

Acknowledgments

Hydrate Ridge sediment samples used here are provided by the Ocean Drilling Program sponsored by the U.S. National Science Foundation and participating countries under the Joint Oceanographic Institutions. We greatly appreciate the support and help in sample distribution given by the curator, John Firth, and the curatorial assistant, Daniel Rohmer, of the IODP Gulf Coast Repository. We thank Liwen Qiu (Nanjing University) for iron analysis and Yiping Chen (East China Institute of Technology) for stable sulfur isotope analysis. We appreciate the valuable suggestions from Dr. Xian-Cai Lu (Nanjing University) and Dr. Simon W. Poulton (University of Leeds). Thanks would also be given to reviewers for their valuable comments and suggestions, which significantly improved the manuscript.

Conflict of interest

The authors declare that the research was conducted in the absence of any commercial or financial relationships that could be construed as a potential conflict of interest.

Publisher's note

References

Aharon, P., and Fu, B. (2000). Microbial sulfate reduction rates and sulfur and oxygen isotope fractionations at oil and gas seeps in deepwater Gulf of Mexico. *Geochim. Cosmochim. Acta* 64, 233–246. doi: 10.1016/S0016-7037(99)00292-6

Aller, R. C., Madrid, V., Chistoserdov, A., Aller, J. Y., and Heilbrun, C. (2010). Unsteady diagenetic processes and sulfur biogeochemistry in tropical deltaic muds: Implications for oceanic isotope cycles and the sedimentary record. *Geochim. Cosmochim. Acta* 74, 4671–4692. doi: 10.1016/j.gca.2010.05.008

Aplin, A. C., Macquaker, J. H. S., Lovley, D. R., Meadows, P., Small, J., Lyons, T., et al. (1993). C-S-Fe geochemistry of some modern and ancient anoxic marine muds and mudstones [and discussion]. *Philos. Trans. R. Soc London Ser. A* 344, 89–100. doi: 10.1098/rsta.1993.0077

Backlund, K., Boman, A., Fröjdö, S., and Åström, M. (2005). An analytical procedure for determination of sulphur species and isotopes in boreal acid sulphate soils and sediments. *Agr. Food Sci.* 14, 70–82. doi: 10.2137/1459606054224147

Bangs, N. L. B., Musgrave, R. J., and Tréhu, A. M. (2005). Upward shifts in the southern Hydrate Ridge gas hydrate stability zone following postglacial warming, offshore Oregon. *J. Geophys. Res.* 110, B03102. doi: 10.1029/2004JB003293

Barnes, R. O., and Goldberg, E. D. (1976). Methane production and consumption in anoxic marine sediments. *Geology* 4, 297–300.

Bates, A. L., Spiker, E. C., Orem, W. H., and Burnett, W. C. (1993). Speciation and isotopic composition of sulfur in sediments from Jellyfish Lake, Palau. *Chem. Geol.* 106, 63–76. doi: 10.1016/0009-2541(93)90166-G

Beaudoin, G., Taylor, B. E., Rumble Iii, D., and Thiemens, M. (1994). Variations in the sulfur isotope composition of troilite from the Cañon Diablo iron meteorite. *Geochim. Cosmochim. Acta* 58, 4253–4255. doi: 10.1016/0016-7037(94)90277-1

Berner, R. A. (1970). Sedimentary pyrite formation. *Am. J. Sci.* 268, 1–23. doi: 10.2475/ajs.268.1.1

Berner, R. A. (1981). A new geochemical classification of sedimentary environments. *J. Sed. Res.* 51, 359–365. doi: 10.1306/212f7c7f-2b24-11d7-8648000102c1865d

Boetius, A., Ravenschlag, K., Schubert, C. J., Rickert, D., Widdel, F., Gieseke, A., et al. (2000). A marine microbial consortium apparently mediating anaerobic oxidation of methane. *Nature* 407, 623–626. doi: 10.1038/35036572

Borowski, W. S. (2006). "Data report: Dissolved sulfide concentration and sulfur isotopic composition of sulfide and sulfate in pore waters, ODP Leg 204, Hydrate Ridge and vicinity, Cascadia margin, offshore Oregon," in *Proc. ODP, Sci. Results*. Eds. A. M. Tréhu, G. Bohrmann, M. E. Torres and F. S. Colwell (Ocean Drilling Program, College Station, TX), 1–13. doi: 10.2973/odp.proc.sr.204.105.2006

Borowski, W. S., Paull, C. K., and Ussler Iii, W. (1996). Marine pore-water sulfate profiles indicate in *situ* methane flux from underlying gas hydrate. *Geology* 24, 655–658.

Borowski, W. S., Rodriguez, N. M., Paull, C. K., and Ussler Iii, W. (2013). Are ^{34}S-enriched authigenic sulfide minerals a proxy for elevated methane flux and gas hydrates in the geologic record? *Mar. Petrol. Geol.* 43, 381–395. doi: 10.1016/j.marpetgeo.2012.12.009

Böttcher, M. E., Smock, A. M., and Cypionka, H. (1998). Sulfur isotope fractionation during experimental precipitation of iron(II) and manganese(II) sulfide at room temperature. *Chem. Geol.* 146, 127–134. doi: 10.1016/S0009-2541(98)00004-7

Böttcher, M. E., Thamdrup, B., and Vennemann, T. W. (2001). Oxygen and sulfur isotope fractionation during anaerobic bacterial disproportionation of elemental sulfur. *Geochim. Cosmochim. Acta* 65, 1601–1609. doi: 10.1016/S0016-7037(00)00628-1

Bottrell, S. H., Parkes, R. J., Cragg, B. A., and Raiswell, R. (2000). Isotopic evidence for anoxic pyrite oxidation and stimulation of bacterial sulphate reduction in marine sediments. *J. Geol. Soc London* 157, 711–714. doi: 10.1144/jgs.157.4.711

Canfield, D. E. (1989). Reactive iron in marine sediments. *Geochim. Cosmochim. Acta* 53, 619–632. doi: 10.1016/0016-7037(89)90005-7

Canfield, D. E., Raiswell, R., and Bottrell, S. H. (1992). The reactivity of sedimentary iron minerals toward sulfide. *Am. J. Sci.* 292, 659–683. doi: 10.2475/ajs.292.9.659

Canfield, D. E., Raiswell, R., Westrich, J. T., Reaves, C. M., and Berner, R. A. (1986). The use of chromium reduction in the analysis of reduced inorganic sulfur in sediments and shales. *Chem. Geol.* 54, 149–155. doi: 10.1016/0009-2541(86)90078-1

Canfield, D., and Thamdrup, B. (1994). The production of ^{34}S-depleted sulfide during bacterial disproportionation of elemental sulfur. *Science* 266, 1973–1975. doi: 10.1126/science.11540246

Chatterjee, S., Dickens, G. R., Bhatnagar, G., Chapman, W. G., Dugan, B., Snyder, G. T., et al. (2011). Pore water sulfate, alkalinity, and carbon isotope profiles in shallow sediment above marine gas hydrate systems: A numerical modeling perspective. *J. Geophys. Res.* 116, B09103. doi: 10.1029/2011jb008290

Chevallier, J., Tréhu, A. M., Bangs, N. L., Johnson, J. E., and Meyer, H. J. (2006). "Seismic sequence stratigraphy and tectonic evolution of southern Hydrate Ridge," in *Proc. ODP, Sci. Results*. Eds. A. M. Tréhu, G. Bohrmann, M. E. Torres and F. S. Colwell (Ocean Drilling Program, College Station, TX), 1–29. doi: 10.2973/odp.proc.sr.204.121.2006

Claypool, G. E., Milkov, A. V., Lee, Y.-J., Torres, M. E., Borowski, W. S., and Tomaru, H. (2006). "Microbial methane generation and gas transport in shallow sediments of an accretionary complex, southern Hydrate Ridge (ODP Leg 204), offshore Oregon, USA," in *Proc. ODP, Sci. Results*. Eds. A. M. Tréhu, G. Bohrmann, M. E. Torres and F. S. Colwell (Ocean Drilling Program, College Station, TX), 1–52. doi: 10.2973/odp.proc.sr.204.113.2006

Cornwell, J. C., and Morse, J. W. (1987). The characterization of iron sulfide minerals in anoxic marine sediments. *Mar. Chem.* 22, 193–206. doi: 10.1016/0304-4203(87)90008-9

De Lange, G. J. (1983). Geochemical evidence of a massive slide in the southern Norwegian Sea. *Nature* 305, 420–422. doi: 10.1038/305420a0

Devol, A. H., and Ahmed, S. I. (1981). Are high rates of sulphate reduction associated with anaerobic oxidation of methane? *Nature* 291, 407–408. doi: 10.1038/291407a0

Dickens, G. R. (2001). Sulfate profiles and barium fronts in sediment on the Blake Ridge: Present and past methane fluxes through a large gas hydrate reservoir. *Geochim. Cosmochim. Acta* 65, 529–543. doi: 10.1016/S0016-7037(00)00556-1

Ding, T.-P., Vaikiers, S., Wan, D.-F., Bai, R.-M., Zou, X.-Q., Li, Y.-H., et al. (2001). The δ^{33}S and δ^{34}S values and absolute ^{32}S/^{33}S and ^{32}S/^{34}S ratios of IAEA and Chinese sulfur isotope reference materials. *Bull. Mineral. Petrol. Geochem.* 20, 425–427.

Dominguez, A. R., and van der Voo, R. (2014). Secular variation of the middle and late Miocene geomagnetic field recorded by the Columbia River Basalt Group in Oregon, Idaho and Washington, USA. *Geophys. J. Int.* 197, 1299–1320. doi: 10.1093/gji/ggt487

Fossing, H., Ferdelman, T. G., and Berg, P. (2000). Sulfate reduction and methane oxidation in continental margin sediments influenced by irrigation (South-East Atlantic off Namibia). *Geochim. Cosmochim. Acta* 64, 897–910. doi: 10.1016/S0016-7037(99)00349-X

Froelich, P. N., Klinkhammer, G. P., Bender, M. L., Luedtke, N. A., Heath, G. R., Cullen, D., et al. (1979). Early oxidation of organic matter in pelagic sediments of the eastern equatorial Atlantic: Suboxic diagenesis. *Geochim. Cosmochim. Acta* 43, 1075–1090. doi: 10.1016/0016-7037(79)90095-4

Fu, Y., Von Dobeneck, T., Franke, C., Heslop, D., and Kasten, S. (2008). Rock magnetic identification and geochemical process models of greigite formation in Quaternary marine sediments from the Gulf of Mexico (IODP Hole U1319A). *Earth Planet. Sci. Lett.* 275, 233–245. doi: 10.1016/j.epsl.2008.07.034

Goldfinger, C., Kulm, L. D., Yeats, R. S., Hummon, C., Huftile, G. J., Niem, A. R., et al. (1996). "Oblique strike-slip faulting of the Cascadia submarine forearc: The Daisy Bank fault zone off central Oregon," in *Subduction: top to bottom: AGU geophysical monograph*. Eds. G. E. Bebout, D. W. Scholl, S. H. Kirby and J. P. Platt (American Geophysical Union, Washington, DC), 65–74.

Goldhaber, M. B. (2003). "Sulfur-rich sediments," in *Treatise on geochemistry*. Eds. H. D. Holland and K. K. Turekian (Elsevier-Pergamon, Oxford), 257–288. doi: 10.1016/B0-08-043751-6/07139-5

Goldhaber, M. B., and Kaplan, I. R. (1974). "The sulfur cycle," in *The sea; ideas and observations on progress in the study of the seas*. Ed. E. D. Goldberg (Wiley-Interscience, New York), 569–655.

Goldhaber, M. B., and Kaplan, I. R. (1975). Controls and consequences of sulfate reduction rates in recent marine sediments. *Soil Sci.* 119, 42–55.

Gröger, J., Franke, J., Hamer, K., and Schulz, H. D. (2009). Quantitative recovery of elemental sulfur and improved selectivity in a chromium-reducible sulfur distillation. *Geostand. Geoanal. Res.* 33, 17–27. doi: 10.1111/j.1751-908X.2009.00922.x

Harrison, A. G., and Thode, H. G. (1958). Mechanism of the bacterial reduction of sulphate from isotope fractionation studies. *Trans. Faraday Soc* 54, 84–92. doi: 10.1039/TF9585400084

Hensen, C., Zabel, M., Pfeifer, K., Schwenk, T., Kasten, S., Riedinger, N., et al. (2003). Control of sulfate pore-water profiles by sedimentary events and the significance of anaerobic oxidation of methane for the burial of sulfur in marine sediments. *Geochim. Cosmochim. Acta* 67, 2631–2647. doi: 10.1016/S0016-7037(03)00199-6

Horng, C.-S., and Chen, K.-H. (2006). Complicated magnetic mineral assemblages in marine sediments offshore of southwestern Taiwan: Possible influence of methane flux on the early diagenetic process. *Terr. Atmos. Oceanic Sci.* 17, 1009–1026.

Iversen, N., and Jørgensen, B. B. (1985). Anaerobic methane oxidation rates at the sulfate-methane transition in marine sediments from Kattegat and Skagerrak (Denmark). *Limnol. Oceanogr.* 30, 944–955. doi: 10.4319/lo.1985.30.5.0944

Johnson, J. E., Goldfinger, C., Tréhu, A. M., Bangs, N. L. B., Torres, M. E., and Chevallier, J. (2006). "North-south variability in the history of deformation and fluid venting across Hydrate Ridge, Cascadia margin," in *Proc. ODP, Sci. Results*. Eds. A. M. Tréhu, G. Bohrmann, M. E. Torres and F. S. Colwell (Ocean Drilling Program, College Station, TX), 1–16. doi: 10.2973/odp.proc.sr.204.125.2006

Jørgensen, B. B. (1979). A theoretical model of the stable sulfur isotope distribution in marine sediments. *Geochim. Cosmochim. Acta* 43, 363–374. doi: 10.1016/0016-7037(79)90201-1

Jørgensen, B. B., Böttcher, M. E., Lüschen, H., Neretin, L. N., and Volkov, I. I. (2004). Anaerobic methane oxidation and a deep H_2S sink generate isotopically heavy sulfides in Black Sea sediments. *Geochim. Cosmochim. Acta* 68, 2095–2118. doi: 10.1016/j.gca.2003.07.017

Jørgensen, B., and Kasten, S. (2006). "Sulfur cycling and methane oxidation," in *Marine geochemistry, 2nd*. Eds. H. Schulz and M. Zabel (Springer-Verlag, Berlin Heidelberg), 271–309. doi: 10.1007/3-540-32144-6_8

Kao, S.-J., Horng, C.-S., Roberts, A. P., and Liu, K.-K. (2004). Carbon-sulfur-iron relationships in sedimentary rocks from southwestern Taiwan: Influence of geochemical environment on greigite and pyrrhotite formation. *Chem. Geol.* 203, 153–168. doi: 10.1016/j.chemgeo.2003.09.007

Kemp, A. L. W., and Thode, H. G. (1968). The mechanism of the bacterial reduction of sulphate and of sulphite from isotope fractionation studies. *Geochim. Cosmochim. Acta* 32, 71–91. doi: 10.1016/0016-7037(68)90088-4

Larrasoaña, J. C., Gràcia, E., Garcés, M., Musgrave, R. J., Piñero, E., Martínez-Ruiz, F., et al. (2006). "Rock magnetic identification of magnetic iron sulfides and its bearing on the occurrence of gas hydrates, ODP Leg 204 (Hydrate Ridge)," in *Proc. ODP, Sci. Results*. Eds. A. M. Tréhu, G. Bohrmann, M. E. Torres and F. S. Colwell (Ocean Drilling Program, College Station, TX), 1–33. doi: 10.2973/odp.proc.sr.204.111.2006

Larrasoaña, J. C., Roberts, A. P., Musgrave, R. J., Gràcia, E., Piñero, E., Vega, M., et al. (2007). Diagenetic formation of greigite and pyrrhotite in gas hydrate marine sedimentary systems. *Earth Planet. Sci. Lett.* 261, 350–366. doi: 10.1016/j.epsl.2007.06.032

Leeder, M. R. (1999). *Sedimentology and sedimentary basins: from turbulence to tectonics* (Oxford; Malden, MA: Blackwell Science).

Lin, Q., Wang, J., Taladay, K., Lu, H., Hu, G., Sun, F., et al. (2016). Coupled pyrite concentration and sulfur isotopic insight into the paleo sulfate-methane transition zone (SMTZ) in the northern South China Sea. *J. Asian Earth Sci.* 115, 547–556. doi: 10.1016/j.jseaes.2015.11.001

Liu, X., Fike, D., Li, A., Dong, J., Xu, F., Zhuang, G., et al. (2019). Pyrite sulfur isotopes constrained by sedimentation rates: Evidence from sediments on the East China Sea inner shelf since the late Pleistocene. *Chem. Geol.* 505, 66–75. doi: 10.1016/j.chemgeo.2018.12.014

Liu, X., Gu, Y., Dong, J., Li, A., Zhuang, G., and Wang, H. (2023). Iron-bearing minerals indicate sea-level rise of the East China Sea inner shelf since the last deglaciation. *Sci. Bull.* 68, 364–366. doi: 10.1016/j.scib.2023.02.002

Liu, C., Jiang, S.-Y., Su, X., Huang, C.-Y., Zhou, Y., Bian, X., et al. (2019). An effective method to distinguish between artificial and authigenic gypsum in marine sediments. *Mar. Petrol. Geol.* 110, 706–716. doi: 10.1016/j.marpetgeo.2019.07.044

Luo, Y., Su, X., Jiang, S., Liu, C., and Tréhu, A. M. (2013). The magnetic properties of iron sulfide minerals from Hydrate Ridge cores, East Pacific and their significance. *Earth Sci. Front.* 20, 235–247.

Mackay, M. E. (1995). Structural variation and landward vergence at the toe of the Oregon accretionary prism. *Tectonics* 14, 1309–1320. doi: 10.1029/95tc02320

Mackay, M. E., Moore, G. F., Cochrane, G. R., Casey Moore, J., and Kulm, L. D. (1992). Landward vergence and oblique structural trends in the Oregon margin accretionary prism: Implications and effect on fluid flow. *Earth Planet. Sci. Lett.* 109, 477–491. doi: 10.1016/0012-821X(92)90108-8

Nauhaus, K., Boetius, A., Krüger, M., and Widdel, F. (2002). *In vitro* demonstration of anaerobic oxidation of methane coupled to sulphate reduction in sediment from a marine gas hydrate area. *Environ. Microbiol.* 4, 296–305. doi: 10.1046/j.1462-2920.2002.00299.x

Novosel, I., Spence, G. D., and Hyndman, R. D. (2005). Reduced magnetization produced by increased methane flux at a gas hydrate vent. *Mar. Geol.* 216, 265–274. doi: 10.1016/j.margeo.2005.02.027

Paull, C. K., Ussler, W., Greene, H. G., Barry, J., and Keaten, R. (2005). Bioerosion by chemosynthetic biological communities on Holocene submarine slide scars. *Geo-Mar. Lett.* 25, 11–19. doi: 10.1007/s00367-004-0184-z

Poulton, S. W., Krom, M. D., and Raiswell, R. (2004). A revised scheme for the reactivity of iron (oxyhydr)oxide minerals towards dissolved sulfide. *Geochim. Cosmochim. Acta* 68, 3703–3715. doi: 10.1016/j.gca.2004.03.012

Price, F. T., and Shieh, Y. N. (1979). Fractionation of sulfur isotopes during laboratory synthesis of pyrite at low temperatures. *Chem. Geol.* 27, 245–253. doi: 10.1016/0009-2541(79)90042-1

Pye, K., Dickson, J., Schiavon, N., Coleman, M. L., and Cox, M. (1990). Formation of siderite-Mg-calcite-iron sulphide concretions in intertidal marsh and sandflat sediments, north Norfolk, England. *Sedimentology* 37, 325–343. doi: 10.1111/j.1365-3091.1990.tb00962.x

Reeburgh, W. S. (1980). Anaerobic methane oxidation: Rate depth distributions in Skan Bay sediments. *Earth Planet. Sci. Lett.* 47, 345–352. doi: 10.1016/0012-821X(80)90021-7

Rees, C. E., Jenkins, W. J., and Monster, J. (1978). The sulphur isotopic composition of ocean water sulphate. *Geochim. Cosmochim. Acta* 42, 377–381. doi: 10.1016/0016-7037(78)90268-5

Regnier, P., Dale, A. W., Arndt, S., Larowe, D. E., Mogollón, J., and Van Cappellen, P. (2011). Quantitative analysis of anaerobic oxidation of methane (AOM) in marine sediments: A modeling perspective. *Earth-Sci. Rev.* 106, 105–130. doi: 10.1016/j.earscirev.2011.01.002

Reidel, S. P., and Tolan, T. L. (1992). Eruption and emplacement of flood basalt: An example from the large-volume Teepee Butte Member, Columbia River Basalt Group. *Geol. Soc Am. Bull.* 104, 1650–1671.

Rickard, D., and Morse, J. W. (2005). Acid volatile sulfide (AVS). *Mar. Chem.* 97, 141–197. doi: 10.1016/j.marchem.2005.08.004

Roberts, A. P. (2015). Magnetic mineral diagenesis. *Earth-Sci. Rev.* 151, 1–47. doi: 10.1016/j.earscirev.2015.09.010

Roberts, A. P., and Weaver, R. (2005). Multiple mechanisms of remagnetization involving sedimentary greigite (Fe_3S_4). *Earth Planet. Sci. Lett.* 231, 263–277. doi: 10.1016/j.epsl.2004.11.024

Shipboard Scientific Party (2003a). "Leg 204 summary," in *Proc. ODP, Init. Rep.* Eds. A. M. Tréhu, G. Bohrmann, F. R. Rack, M. E. Torres, N. L. Bangs, S. R. Barr, W. S. Borowski, G. E. Claypool, T. S. Collett, M. E. Delwiche, G. R. Dickens, D. S. Goldberg, E. Gràcia, G. Guèrin, M. Holland, J. E. Johnson, Y.-J. Lee, C.-S. Liu, P. E. Long, A. V. Milkov, M. Riedel, P. Schultheiss, X. Su, B. Teichert, H. Tomaru, M. Vanneste, M. Watanabe, J. L. Weinberger and M. Chapman (Ocean Drilling Program, College Station, TX 77845-9547, USA), 1–75. doi: 10.2973/odp.proc.ir.204.101.2003

Shipboard Scientific Party (2003b). "Site 1245," in *Proc. ODP, Init. Rep.* Eds. A. M. Tréhu, G. Bohrmann, F. R. Rack, M. E. Torres, N. L. Bangs, S. R. Barr, W. S. Borowski, G. E. Claypool, T. S Collett, M. E. Delwiche, G. R. Dickens, D. S. Goldberg, E. Gràcia, G. Guèrin, M. Holland, J. E. Johnson, Y.-J. Lee, C.-S. Liu, P. E. Long, A. V. Milkov, M. Riedel, P. Schultheiss, X. Su, B. Teichert, H. Tomaru, M. Vanneste, M. Watanabe, J. L. Weinberger and M. Chapman (Ocean Drilling Program, College Station, TX 77845-9547, USA), 1–131. doi: 10.2973/odp.proc.ir.204.104.2003

Shipboard Scientific Party (2003c). "Site 1252," in *Proc. ODP, Init. Rep.* Eds. A. M. Tréhu, G. Bohrmann, F. R. Rack, M. E. Torres, N. L. Bangs, S. R. Barr, W. S. Borowski, G. E. Claypool, T. S. Collett, M. E. Delwiche, G. R. Dickens, D. S. Goldberg, E. Gràcia, G. Guèrin, M. Holland, J. E. Johnson, Y.-J. Lee, C.-S. Liu, P. E. Long, A. V. Milkov, M. Riedel, P. Schultheiss, X. Su, B. Teichert, H. Tomaru, M. Vanneste, M. Watanabe, J. L. Weinberger and M. Chapman (Ocean Drilling Program, College Station, TX 77845-9547, USA), 1–62. doi: 10.2973/odp.proc.ir.204.111.2003

Strong, M., and Wolff, J. (2003). Compositional variations within scoria cones. *Geology* 31, 143–146. doi: 10.1130/0091-7613(2003)031<0143:cvwsc>2.0.co;2

Sweeney, R. E., and Kaplan, I. R. (1973). Pyrite framboid formation: Laboratory synthesis and marine sediments. *Econ. Geol.* 68, 618–634. doi: 10.2113/gsecongeo.68.5.618

Teichert, B. M. A., and Bohrmann, G. (2006). "Data report: Composition of authigenic carbonates in sediments of the Cascadia accretionary prism, ODP Leg 204," in *Proc. ODP, Sci. Results*. Eds. A. M. Tréhu, G. Bohrmann, M. E. Torres and F. S. Colwell (Ocean Drilling Program, College Station, TX), 1–8. doi: 10.2973/odp.proc.sr.204.116.2006

Teichert, B. M. A., Eisenhauer, A., Bohrmann, G., Haase-Schramm, A., Bock, B., and Linke, P. (2003). U/Th systematics and ages of authigenic carbonates from Hydrate Ridge, Cascadia Margin: Recorders of fluid flow variations. *Geochim. Cosmochim. Acta* 67, 3845–3857. doi: 10.1016/S0016-7037(03)00128-5

Torres, M. E., Teichert, B. M. A., Tréhu, A. M., Borowski, W., and Tomaru, H. (2004). Relationship of pore water freshening to accretionary processes in the Cascadia margin: Fluid sources and gas hydrate abundance. *Geophys. Res. Lett.* 31, L22305. doi: 10.1029/2004gl021219

Tréhu, A. M., Bohrmann, G., Rack, F. R., Torres, M. E N., Bangs, L., Barr, S. R., et al. (Eds.) (2003). *Proceedings of the ocean drilling program; initial reports* (College Station, TX 77845-9547, USA: Ocean Drilling Program).

Tréhu, A. M., Bohrmann, G., Torres, M. E., and Colwell, F. S. (2006a). *Proceedings of the ocean drilling program; scientific results* (College Station, TX: Ocean Drilling Program).

Tréhu, A. M., Long, P. E., Torres, M. E., Bohrmann, G., Rack, F. R., Collett, T. S., et al. (2004). Three-dimensional distribution of gas hydrate beneath southern Hydrate Ridge: Constraints from ODP Leg 204. *Earth Planet. Sci. Lett.* 222, 845–862. doi: 10.1016/j.epsl.2004.03.035

Tréhu, A. M., Torres, M. E., Bohrmann, G., and Colwell, F. S. (2006b). "Leg 204 synthesis: Gas hydrate distribution and dynamics in the central Cascadia accretionary complex," in *Proc. ODP, Sci. Results*. Eds. A. M. Tréhu, G. Bohrmann, M. E. Torres and F. S. Colwell (Ocean Drilling Program, College Station, TX), 1–40. doi: 10.2973/odp.proc.sr.204.101.2006

Tréhu, A. M., Torres, M. E., Moore, G. F., Suess, E., and Bohrmann, G. (1999). Temporal and spatial evolution of a gas hydrate-bearing accretionary ridge on the Oregon continental margin. *Geology* 27, 939–942.

Treude, T., Boetius, A., Knittel, K., Wallmann, K., and Jørgensen, B. B. (2003). Anaerobic oxidation of methane above gas hydrates at Hydrate Ridge, NE Pacific Ocean. *Mar. Ecol. Prog. Ser.* 264, 1–14. doi: 10.3354/meps264001

Watanabe, M. (2006). "Data report: Diatom biostratigraphy of Sites 1251 and 1252," in *Proc. ODP, Sci. Results*. Eds. A. M. Trehu, G. Bohrmann, M. E. Torres and F. S. Colwell (Ocean Drilling Program, College Station, TX), 1–10. doi: 10.2973/odp.proc.sr.204.123.2006

Wilkin, R. T., and Barnes, H. L. (1996). Pyrite formation by reactions of iron monosulfides with dissolved inorganic and organic sulfur species. *Geochim. Cosmochim. Acta* 60, 4167–4179. doi: 10.1016/s0016-7037(97)81466-4

Yamaguchi, K. E., Johnson, C. M., Beard, B. L., Ohmoto, H., and Nealson, K. H. (2005). "Isotopic evidence for 3 billion years of bacterial redox cycling of iron," in *Frontier research on earth evolution (IFREE report for 2003-2004)*. Ed. Y. Fukao (Japan Agency for Marine-Earth Science and Technology, Yokosuka), 1–8.

Zabel, M., and Schulz, H. D. (2001). Importance of submarine landslides for non-steady state conditions in pore water systems — lower Zaire (Congo) deep-sea fan. *Mar. Geol.* 176, 87–99. doi: 10.1016/s0025-3227(01)00164-5